Comprehensive evaluation of typical planetary boundary layer (PBL) parameterization schemes in China. Part I: Understanding expressiveness of schemes for different regions from the mechanism perspective

Wenxing Jia[1], Xiaoye Zhang[1,2*], Hong Wang[1], Yaqiang Wang[1], Deying Wang[1], Junting Zhong[1], Wenjie Zhang[1], Lei Zhang[1], Lifeng Guo[1], Yadong Lei[1], Jizhi Wang[1], Yuanqin Yang[1], Yi Lin[3]

[1]State Key Laboratory of Severe Weather & Key Laboratory of Atmospheric Chemistry of CMA, Chinese Academy of Meteorological Sciences, Beijing, 100081, China

[2]Center for Excellence in Regional Atmospheric Environment, IUE, Chinese Academy of Sciences, Xiamen, 361021, China

[3]Key Laboratory for Mesoscale Severe Weather, Ministry of Education, and School of Atmospheric Sciences, Nanjing University, Nanjing, 210023, China

Correspondence to: X. Zhang (xiaoye@cma.gov.cn)

Abstract. The optimal choice of the planetary boundary layer (PBL) parameterization scheme is of particular interest and urgency to a wide range of scholars, especially for many works involving models. At present, there have been many works to evaluate the PBL schemes. However, little research has been conducted into a more comprehensive and systematic assessment of the performance capability of schemes in key regions of China, especially when it comes to the differences in the mechanisms of the schemes themselves, primarily because there's scarcely sufficient observational data, computer resources, and storage support to complete the work. ~~In addition, there are many factors that influence the selection of schemes, such as underlying surface, initial and boundary conditions, near surface layer scheme, horizontal/vertical resolution, etc.~~ In this Part (i.e., Part I), four typical schemes (i.e., YSU, ACM2, BL and MYJ) are selected to systematically analyze and evaluate near-surface meteorological parameters, PBL vertical structure, PBL height (PBLH), and turbulent diffusion coefficient (TDC) in five key regions (i.e., North China Plain, NCP; Yangtze River Delta, YRD; Sichuan Basin, SB; Pearl River Delta, PRD and Northwest Semi-arid, NS) of China in different seasons (i.e., January, April, July and October). The differences in the simulated 2-m temperatures between the nonlocal closure schemes are mainly affected by the downward shortwave radiation, but to compare the nonlocal closure schemes with the local closure schemes, the effect of sensible heat flux needs to be further considered. ~~In terms of temporal variation, the simulated results for July are better than the other three months, and the simulated results for nighttime are better than daytime. In terms of regional distribution, the temperature at stations with higher elevation is easily underestimated, while overestimated with lower elevation. The variation of relative humidity corresponds to temperature.~~ The 10-m wind speed is under the influence of factors like the momentum transfer coefficient and the integrated similarity functions at night. The wind speeds are more significantly overestimated in the plains and basin, while less overestimated or even underestimated in the mountains, as a result of the effect on topographic smoothing in the model. Moreover, the overestimation of small wind speeds at night is attributable to the inapplicability of the Monin-Obukhov similarity theory (MOST) at night. The model captures the vertical structure of temperature well, while the wind speed is outstandingly overestimated below 1000 m, largely because of the ~~turbulent diffusion coefficient (~~TDC~~)~~. The difference between the MOST and the mixing length theory, PBLH and Prandtl number is cited as the reason for the difference between the TDC of the YSU and ACM2 schemes. The TDCs of the BL and MYJ schemes are affected by the mixing length scale, which of BL is calculated on the basis of the effect of buoyancy, while MYJ calculates it with the consideration of the effect of the total turbulent kinetic energy. The PBLH of the BL scheme is better than the other schemes because of the better simulation results of temperature. ~~The difference in the PBLH by the YSU and ACM2 scheme mainly comes from the Richardson number and the jagged PBLH of the MYJ scheme is due to the coarse vertical resolution and the threshold value.~~

In general, to select the optimal scheme, it is necessary to offer different options for different regions with different focuses (heat or momentum). (1) Temperature field. The BL scheme is recommended for January in the NCP region, especially for Beijing, and the MYJ scheme is better for the other three months. The ACM2 scheme would be a good match for the YRD region, where the simulation differences between the four schemes are small. The topography of the SB region is more complex, but for most of the areas in the basin, the MYJ scheme is proposed, but if more stations outside the basin are involved, the BL scheme is recommended. The MYJ scheme is applied to the PRD region in January and April, and the BL scheme in July and October. The MYJ scheme is counselled for the NS region. (2) Wind field. The YSU scheme is recommended if the main concern is the near-surface layer, and the BL scheme is suggested if focusing on the variation in the vertical direction. ~~The Part II will analyse and evaluate the factors that may influence the choice of the schemes and the results of model.~~ The final evaluation of the parameterization scheme and uncertainties will lay the foundation for the improvement of the modules and forecasting of the GRAPES_CUACE regional model developed independently in China.

1 Introduction

The planetary boundary layer (PBL) is the part of the troposphere that is directly influenced by the force of the earth's surface with an hour or less timescale(R. B. Stull, 1988). Parameterization is the determining factor in the predictive accuracy and skill as it determines key aspects of simulated weather(Bauer et al., 2015; Williams, 2005). In numerical weather prediction, meagre computational resources limit the resolution of the model. Following this reason, physical processes cannot be resolved by the model in that the spatial scales are smaller than the model grid distance. The physical module in the model that characterizes small scales relative to the model resolution is called the sub-grid physical process parameterization scheme(Zhou et al., 2017). As a typical sub-grid parameterization scheme, the spatial scale of turbulence is limited by the PBL height (PBLH) and cannot be resolved by mesoscale weather prediction models and macroscale global climate models with horizontal grid distances of magnitude of ~10 km and ~100 km. Therefore, the physical module in the model that describes the effect of sub-grid turbulence on resolvable atmospheric motion is called the PBL parameterization scheme. Even in the high resolution large-eddy simulation (LES), small-scale turbulence requires parametric closure to characterize the role of sub-grid turbulence(Deardorff, 1980). The PBL parameterization scheme controls the evolution of momentum, heat, water vapor, and mass within the PBL, and the evolution of these parameters is particularly affected by the turbulent diffusion coefficients (TDCs)(W. Jia and Zhang, 2021; Nielsen-Gammon et al., 2010; Oke et al., 2017). Depending on the turbulence closure method, the PBL parameterization schemes can be divided into three main categories: nonlocal closure schemes,

104   local closure schemes, and hybrid nonlocal-local closure schemes, and the above schemes have their

105   own advantages and disadvantages(Cohen et al., 2015; Hu et al., 2010; Wenxing Jia and Zhang,

106   2020; Xie et al., 2012).

107   Since the early 1980s, the vertical diffusion scheme based on local gradients of wind and potential

108   temperature (i.e., local K-theory) has been applied in the National Centers for Environmental

109   Prediction (NCEP). However, as pointed out by many scholars, this scheme has many deficiencies,

110   of which the most critical is that the mass and momentum transport within the PBL is mainly

111   accomplished by the large-scale eddies besides the local small-scale eddies(Roland B. Stull, 1984;

112   Wyngaard and Brost, 1984). Therefore, the new scheme developed later incorporates a counter-

113   gradient flux term to characterize the turbulent transport processes in large-scale eddies, such as

114   Medium-Range Forecast (MRF) scheme (i.e., nonlocal closure) (Hong and Pan, 1996; Troen and

115   Mahrt, 1986). This scheme has also been commonly used in China's self-developed

116   Global/Regional Assimilation and PrEdiction System (GRAPES) model because of its

117   computational simplicity and its ability to produce plausible results under typical atmospheric

118   conditions (Ma et al., 2021). Nevertheless, the MRF scheme has gradually shown some

119   shortcomings, the most typical being that when the wind speed is strong, the resulting mixing is too

120   strong and thus the PBLH is too high to be realistic(Mass et al., 2002; Persson et al., 2001). To

121   overcome this critical problem, one of the most commonly used and popular PBL parameterization

122   scheme has been introduced, which is the Yonsei University (YSU) scheme(Hong et al., 2006). YSU

123   scheme adds an additional entrainment term to the MRF scheme for explicitly calculating the

124   entrainment process of heat and momentum fluxes(Noh et al., 2003). It is still unclear why this

125   scheme is popular among scholars, either because it gives the best simulation results or simply

126   because the code of this scheme is 1, which is more convenient for the model setting. To be contrast,

127   a newer scheme, as a nonlocal scheme of the same series, has been developed that further considers

128   the issue of gray-zone of sub-grid scale turbulence, but this scheme has been rarely used and

129   evaluated (Hong and Shin, 2013).

130   Repairing the defects of local K-theory is possible by developing nonlocal closure schemes on the

131   one hand, and higher-order local closure method on the other hand. The most representative is the

132   higher-order closure scheme of the M-Y series proposed by Mellor and Yamada, such as Mellor-

133   Yamada-Janjic (MYJ) scheme and Mellor-Yamada Nakanishi and Niino Level 2.5/3

134   (MYNN2/MYNN3) scheme(Janjić, 1990, 1994; Mellor and Yamada, 1974, 1982; Nakanishi and

135   Niino, 2004). The higher-order closure schemes are capable of representing a well mixing PBL

136   structure, however, these schemes are computationally more expensive due to the addition of a

137   prognostic turbulent kinetic energy (TKE). In addition to the widely used local closure schemes of

138   the M-Y series, there is another local closure scheme that has been evaluated extensively. This

139   scheme is the Bougeault and Lacarrere (BL) scheme(Bougeault and Lacarrere, 1989), but there are

several differences between the BL and M-Y schemes. (1) In the parameterization of the turbulent heat flux, an additional counter-gradient flux term is taken into account in the convective PBL, but this counter-gradient term is different from that in the nonlocal closure scheme, which is a constant $(= 0.7 \cdot 10^{-5} \ K \ cm^{-1})$ in the BL scheme. (2) The turbulent diffusion coefficient in the BL scheme is calculated similarly to the M-Y schemes, but the stability functions and mixing length are different from M-Y schemes.

In addition to the typical nonlocal closure schemes and local closure schemes, there are also hybrid nonlocal-local closure schemes, typically represented by the Asymmetric Convective Model version 2 (ACM2) scheme. ACM2 scheme operates based on the development of ACM1 that is modified based upon the Blackadar convective model(Blackadar, 1962). The upward transport within the PBL is mainly by buoyancy, which is transmitted upward from the lowest level to other levels, while downward is transported level-by-level(Pleim, 2007). The deficiency of the ACM1 scheme is that upward transport is not better represented when the vertical resolution of the model increases. In response to compensating for the shortcomings of the ACM1 scheme, the ACM2 scheme adds level-by-level transport to the upward level. The ACM2 scheme have the highest universality and was most suitable for the study of meteorological elements in desert region(Meng Lu et al., 2018; Wang et al., 2017).

At present, a total of 12 PBL parameterization schemes have been developed and evaluated in the currently popular mesoscale Weather Research and Forecasting (WRF) model. The continuous improvement of numerical simulation techniques brings opportunities for the update and development of PBL parameterization schemes. Many scholars hope that by comparing the PBL parameterization schemes, they can select one scheme that better reflects the changes in meteorological parameters (e.g., temperature, relative humidity and wind speed/direction), pollutants and the structures of the PBL. Recent review studies have shown that although many studies on the evaluation and comparison of PBL parameterization schemes have been undertaken, there is still no uniform conclusion on which PBL parameterization scheme performs best(Wenxing Jia and Zhang, 2020). Moreover, most of the evaluation work on PBL parameterization schemes is done for individual cases or a particular region(Avolio et al., 2017; Diaz et al., 2021; Falasca et al., 2021; Ferrero et al., 2018; He et al., 2022; Shen et al., 2022). In spite of those, simulation results for the PBL parameterization schemes are more uniform: (1) the simulation of temperature is better than that of relative humidity, and the simulation of wind speed and direction is worse. (2) The simulation results of the nonlocal closure scheme are better under unstable conditions, while the local closure scheme for stable conditions. However, these general conclusions are open to speculation and debate(Wenxing Jia and Zhang, 2020). Many previous studies have been biased towards the assessment of basic meteorological parameters, of course, which is the basic work. Due to the indirect output of TDC by the model, there are fewer relevant studies to investigate the impacts

176 of turbulent diffusion on meteorological parameters. Moreover, turbulent diffusion is the key factor
177 to control the vertical mixing of momentum and scalars within the PBL. Even if there is not enough
178 turbulence observation data, it can be further analyzed and discussed according to the simulation
179 results. Considering that every type of parameterization scheme should be covered, aAimed at
180 remedying the current research deficiencies, this study first selects four typical boundary layer
181 parameterization schemes (nonlocal scheme: YSU, local scheme: MYJ and BL, hybrid nonlocal-
182 local scheme: ACM2) for five typical regions (NCP, YRD, SB, PRD and NS) in China, and then
183 assesses the performance capability of different PBL parameterization schemes in different regions.
184 The reasons for the differences in performance of meteorological parameters between observation
185 and simulation are illustrated in terms of temporal and regional variability. Then, the mechanistic
186 implications behind the differences are explored between schemes. In addition, we further carry out
187 the comparative analysis of the vertical structure of the PBL, turbulent diffusion and the PBLH. The
188 first part of this study (i.e., Part I) aims to be able to have a qualitative and quantitative assessment
189 of the PBL parameterization schemes in different regions for other researchers to use as a reference
190 when doing simulation studies. The second part (i.e., Part II) focuses on the analysis of some
191 uncertain factors that may affect the model simulation results, chiefly including: the influence of
192 meteorological initial and boundary conditions, underlying surface (mainly considering the impact
193 of urban and water bodies), near-surface layer (N-SL) scheme (the PBL and N-SL schemes must
194 match each other), the effect of model version update, the influence of regional horizontal and
195 vertical resolution, etc. We hope that we can dissect the effect of uncertainties from some aspects
196 that we are concerned about.

197 **2 Data and methods**

198 **2.1 Data**

199 ***Hourly meteorological observation data.*** The China Meteorological Administration (CMA) has
200 over 2400 automatic weather stations (AWSs), and the stations record variables such as temperature,
201 relative humidity, pressure, wind speed, wind direction and precipitation amount. In the NCP, YRD,
202 SB, PRD, NS regions, 576 stations, 455 stations, 341 stations, 128 stations, and 55 stations have
203 been selected, respectively (illustrated by gray cross in Fig. 1b-f). Observational data for four
204 months January, April, July and October 2016 have been selected and comparatively analyzed.
205 ***L-band radiosonde observation data.*** A total of 120 observation stations are equipped with L-band
206 radiosonde systems in China, which provide fine-resolution (1 Hz, and the rise rate is ~6 m s^{-1})
207 vertical profiles of temperature, relative humidity and wind speed and direction three times (08:00,
208 14:00 and 20:00 Beijing Time, BJT) a day (illustrated by red triangle in Fig. 1b-f). The accuracy of
209 temperature within the lower troposphere is comparable to that of GPS RS 92 radiosonde, which is

210 less than 0.1 K(Miao et al., 2018). Four sounding stations have been selected for each region,
211 including different underlying surface conditions as much as possible. In the NCP region, two plain
212 stations (Beijing: 116.28°E, 39.48°N; 31.3 m above sea level (a.s.l.) and Xingtai: 114.22°E, 37.11°
213 N; 183.0 m a.s.l.) and two mountain stations (Zhangjiakou: 114.55°E, 40.46°N; 771.0 m a.s.l. and
214 Zhangqiu: 117.33°E, 36.41°N; 121.8 m a.s.l.) have been picked. In the YRD region, one station
215 closer to the ocean (Shanghai: 121.27°E, 31.24°N; 5.5 m a.s.l.), two stations with complex
216 underlying surface (Anqing: 116.58°E, 30.37°N; 62.0 m a.s.l. and Quzhou: 118.54°E, 29.00°N; 82.0
217 m a.s.l.), and one plain station (Nanjing: 118.54°E, 31.56°N; 32.0 m a.s.l.) have been opted. In the
218 SB region, three in-basin stations (Wenjiang: 103.52°E, 30.45°N; 549.0 m a.s.l., Shapingba: 106.24°
219 E, 29.36°N; 541.1 m a.s.l. and Daxian: 107.30°E, 31.12°N; 344.0 m a.s.l.) and one out-of-basin
220 station (Hongyuan: 102.33°E, 32.48°N; 3491.6 m a.s.l., with an altitude of 3491 m) have been
221 selected. In the PRD region, two plain stations (Qingyuan: 113.05°E, 23.42°N; 78.0 m a.s.l. and
222 Heyuan: 114.44°E, 23.47°N; 60.0 m a.s.l.) and two stations (Yangjiang: 111.58°E, 21.50°N; 85.0 m
223 a.s.l. and Shantou: 116.41°E, 23.23°N; 2.3 m a.s.l.) closer to the ocean have been singled out. In the
224 NS region, along the Qilian mountains, four stations have been chosen, Mazongshan (97.02°E,
225 41.48°N), with an altitude of 1770 m, Jiuquan (98.29°E, 39.46°N), with an altitude of 1477 m,
226 Zhangye (100.17°E, 39.05°N), with an altitude of 1460 m, and Minqin (103.05°E, 38.38°N), with
227 an altitude of 1367 m.

228 **2.2 Model settings**

229 In this study, we adopt the model WRF-ARW (Advanced Research Weather Research and
230 Forecasting) version 3.9.1 to evaluate the performance of PBL schemes. Long-term three-
231 dimensional simulation experiments are conducted in 1 month of each season of 2016 (i.e., January,
232 April, July and October). Seven nested domains (D1, D2, D3, D4, D5, D6 and D7) are defined (Fig.,
233 1a), with horizontal grid spacings of 75 km (74 × 74 grid cells, 9°N -59°N, 61°E -146°E), 15 km
234 (281 × 281 grid cells, 13°N -51°N, 77°E -136°E), 3 km (331 × 331 grid cells, 34°N -44°N, 111°E
235 -124°E), 3 km (316 × 356 grid cells, 26°N -34°N, 114°E -126°E), 3 km (331 × 331 grid cells, 25°
236 N -33.5°N, 100°E -110°E), 3 km (236 × 301 grid cells, 18°N -25°N, 110°E -119°E), and 3 km (226
237 × 351 grid cells, 36°N -42.7°N, 94°E -107°E), respectively. Along the vertical direction, 48 vertical
238 layers are configured blow the top, and the model top is set to the 50 hPa. To resolve the PBL
239 structure finely, 21 vertical layers are set below 2 km (i.e., the specific setting of vertical levels is σ
240 = 1.000, 0.997, 0.994, 0.991, 0.988, 0.985, 0.980, 0.975, 0.970, 0.960, 0.950, 0.940, 0.930, 0.920,
241 0.910, 0.895, 0.880, 0.865, 0.850, 0.825, 0.800). The initial and boundary conditions of
242 meteorological fields are set up by using the NCEP Global Forecast System (GFS) Final (FNL)
243 gridded analysis datasets, with a resolution of 1° × 1° (https://rda.ucar.edu/datasets/ds083.2/, last
244 access: 4 August, 2022). The Moderate Resolution Imaging Spectroradiometer (MODIS) dataset

245 includes 20 land-use categories(Broxton et al., 2014). The physical parameterization used in the

246 present model is listed in Table 1.
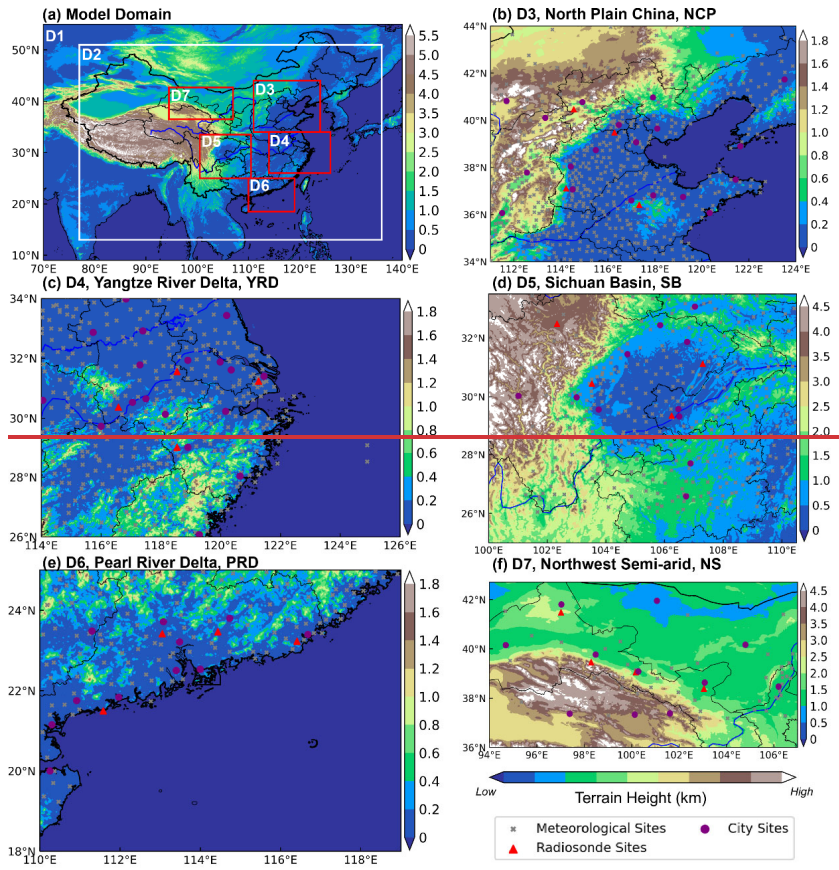
247
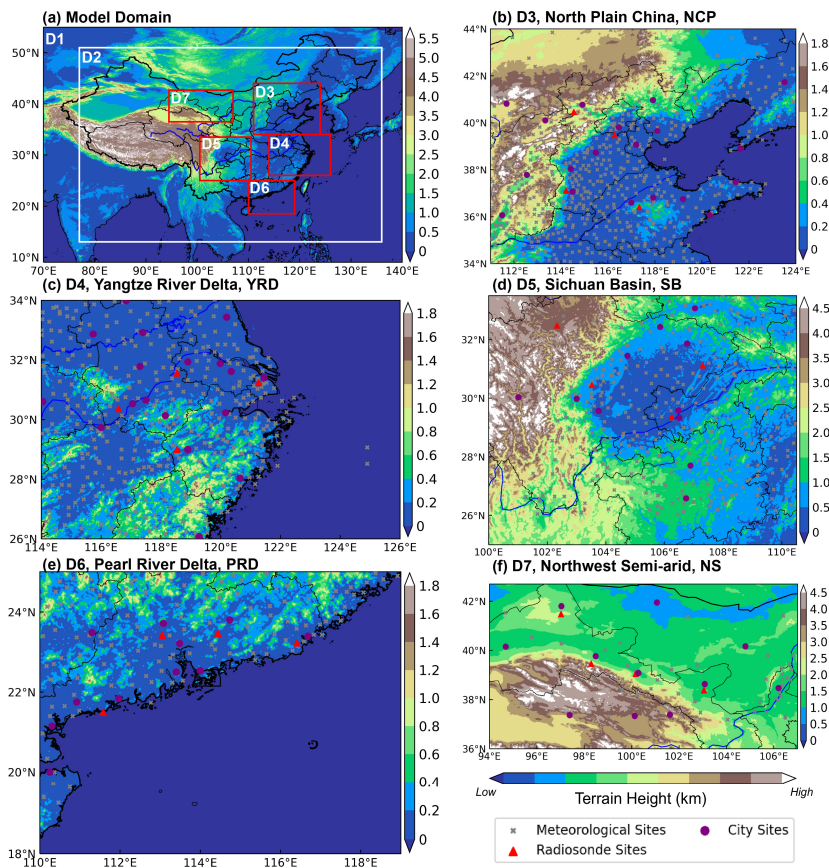
248

249 Figure 1. (a) Map of terrain height in the seven nested model domains. (b-f) Domain 3-7 correspond

250 to the North Plain China (NCP), the Yangtze River Delta (YRD), the Sichuan Basin (SB), the Pearl

251 River Delta (PRD) and the Northwest Semi-arid (NS), respectively. The locations of surface

252 meteorological stations and sounding stations are marked by the gray crosses, red triangles,

253 respectively. The purple dots indicate the major city sites that are our main focus in each region.

254 Table 1. A brief description of the parameterization scheme in the model.

Namelist option	Description	Input option	Reference
mp_physics	Morrison double-moment scheme	10	(Morrison et al., 2009)
ra_lw_physics	RRTMG scheme	4	(Iacono et al., 2008)
ra_sw_physics	RRTMG scheme	4	(Iacono et al., 2008)
cu_physics	Grell-3D scheme	5	(Grell and Dévényi, 2002)
	MM5 similarity scheme	1	(Jiménez and Dudhia, 2012)
sf_sfclay_physics	Monin-Obukhov (Eta) similarity scheme	2	(Janjić, 1994)
sf_surface_physics	Noah land surface	2	(Chen and Dudhia, 2001)

格式化表格

	scheme		
sf_urban_physics	Single-layer UCM scheme	1	(Kusaka et al., 2001)
sf_lake_physics	CLM4.5 lake scheme	1	(Gu et al., 2015)
	YSU scheme	1	(Hong et al., 2006)
	MYJ scheme	2	(Mellor and Yamada, 1982)
bl_pbl_physics	ACM2 scheme	7	(Pleim, 2007)
	BL scheme	8	(Bougeault and Lacarrere, 1989)

All simulations embodied a total of 16 months. The 40 h simulation is conducted beginning from 00:00 UTC of 1d ago for each day (i.e., 492 simulation experiments), the first 16 h of each simulation is considered as the spin-up period, and results obtained from the following 24 h simulations are analyzed for the present study.

2.3 Description of PBL parameterization schemes

2.3.1 YSU scheme

The YSU is a first-order nonlocal scheme with an explicit treatment entrainment process at the top of the PBL:

$$\frac{\partial c}{\partial t} = \frac{\partial}{\partial z}\left[K_c\left(\frac{\partial c}{\partial z} - \gamma_c\right) - \overline{(w'c')}_h\left(\frac{z}{h}\right)^3\right] \quad (1)$$

where c denotes u, v, θ, and the $\gamma_c = b\frac{\overline{(w'c')}_0}{w_{s0}h}$ is the counter-gradient flux term, which increases the nonlocal effect due to the large scale turbulence. z and h are the height of a level of the model and PBLH, respectively. The PBLH is defined by the bulk Richardson number method:

$$h = Rib_{cr}\frac{\theta_{va}|U(h)|^2}{g(\theta_v(h) - \theta_s)} \quad (2)$$

where g is the gravity, and Rib_{cr} is the critical bulk Richardson number, with a value of 0.25 under stable conditions and 0 under unstable conditions. θ_{va} is the virtual potential temperature at the lowest model level, $\theta_v(h)$ is the virtual potential temperature at h, θ_s is the appropriate temperature near the surface ($\theta_s = \theta_{va} + \theta_T$, θ_T is the virtual temperature increment). Compared to the predecessor of the YSU scheme, the entrainment process is additionally treated explicitly (i.e., the last term on the right side of the Eq. (1))

Another key variable is K_c, which is the turbulent diffusion coefficient (TDC), and can be expressed based on the Monin-Obukhov similarity theory (MOST) as:

$$K_c = \frac{\kappa u_* z}{\phi_c}\left(1 - \frac{z}{h}\right)^2 \quad (3)$$

where u_* is the surface frictional velocity and ϕ_c is dimensionless function, the expressions for different stability conditions are:

i.   Unstable and neutral conditions:

280      $\phi_m = \left(1 - 16\frac{0.1h}{L}\right)^{-1/4}$ (4a)

281      $\phi_h = \left(1 - 16\frac{0.1h}{L}\right)^{-1/2}$ (4b)

282   ii.   Stable condition:

283      $\phi_m = \phi_h = \left(1 + 5\frac{0.1h}{L}\right)$ (4c)

284   The TDC of momentum (i.e., K_m) is first calculated in the model, and then the TDC of heat (i.e.,

285   K_h) is calculated, using the Prandtl number (i.e., $Pr = \frac{K_m}{K_h}$). The TDC controls the vertical mixing

286   process of momentum and scalars within the PBL, and it is crucial that it needs to be accurately

287   described.

288   **2.3.2 MYJ scheme**

289   The MYJ scheme is a one-and-a-half order local closure scheme with a prognostic equation for

290   turbulent kinetic energy (TKE, $TKE = e = \frac{1}{2}(u'^2 + v'^2 + w'^2)$):

291      $\frac{\partial \bar{e}}{\partial t} = -\frac{1}{\bar{\rho}}\frac{\partial}{\partial z}\overline{w'p'} - \overline{w'u'}\frac{\partial \bar{u}}{\partial z} - \overline{w'v'}\frac{\partial \bar{v}}{\partial z} - \frac{\partial}{\partial z}\overline{w'e'} + \frac{g}{\theta_v}\overline{w'\theta_v'} - \varepsilon$ (5)

292   The first term on the right side of Eq. (5) is a pressure correlation term which describes TKE is

293   redistributed by pressure perturbations, the second and third terms is a shear production/loss term,

294   the fourth term represents the turbulent transport of TKE, the fifth term describes the buoyant

295   production/consumption term, and the sixth term represents viscous dissipation of TKE. To close

296   the TKE equation, the turbulent fluxes must be parameterized. Based on the gradient transport

297   theory (i.e., K-theory), the turbulent fluxes can be indicated as:

298      $\overline{w'u'} = -K_m\frac{\partial \bar{u}}{\partial z}$ (6a)

299      $\overline{w'v'} = -K_m\frac{\partial \bar{v}}{\partial z}$ (6b)

300      $\overline{w'\theta'} = -K_h\frac{\partial \bar{\theta}}{\partial z}$ (6c)

301   The TDC is proportional to the square root of TKE, and can be expressed as:

302      $K_m = S_m l e^{1/2}$ (7a)

303      $K_h = S_h l e^{1/2}$ (7b)

304   where l is mixing length and can be described as $l = \frac{l_0 \kappa z}{\kappa z + l_0}$, where $l_0 = \alpha\frac{\int_0^\infty z e^{1/2} dz}{\int_0^\infty e^{1/2} dz}$, α is an

305   empirical constant (=0.1). When z converges to a very small value, l converges to κz. However, as

306   z converges to a very large value, l converges to l_0.

307   To obtain the S_m and S_h in Eq. (7), G_m and G_h are defined as:

308     $G_m = \frac{l^2}{2e}\left[\left(\frac{\partial \overline{u}}{\partial z}\right)^2 + \left(\frac{\partial \overline{v}}{\partial z}\right)^2\right]$ (8a)

309     $G_h = -\frac{l^2}{2e}\frac{g}{\theta_v}\frac{\partial \theta_v}{\partial z}$ (8b)

310   S_m and S_h are functions of G_m and G_h, and can be denoted as:

311     $S_m(6A_1A_2G_m) + S_h(1 - 3A_2B_2G_h - 12A_1A_2G_h) = A_2$ (9a)

312     $A_1(1 + 6A_1^2G_m - 9A_1A_2G_h) - S_h(12A_1^2G_h + 9A_1A_2G_h) = A_1(1 - 3C_1)$ (9b)

313   where $[A_1, A_2, B_1, B_2, C_1] = [0.660, 0.657, 11.878, 7.227, 0.001]$.

314   The PBLH in the MYJ scheme is defined as the height at which the TKE is reduced to a critical

315   value of 0.1 m^2 s^{-2}.

316   **2.3.3 ACM2 scheme**

317   Unlike the YSU scheme, the ACM2 scheme applies the transilient matrix to deal with the

318   contribution of nonlocal fluxes. The governing equation can be expressed as:

319     $\frac{\partial C_i}{\partial t} = f_{conv}MuC_1 - f_{conv}Md_iC_i + f_{conv}Md_{i+1}C_{i+1}\frac{\Delta z_{i+1}}{\Delta z_i} + \frac{\partial}{\partial z}\left[K_c(1 - f_{conv})\frac{\partial C_i}{\partial z}\right]$ (10)

320   The first three terms on the right side of Eq. (10) represent nonlocal mixing effect and the fourth

321   term represents local mixing effect. Where C_i is the variable at layer i, Mu is the nonlocal upward

322   convective mixing rate, Md_i is the downward mixing rate from layer i to layer i-1, Δz_i is the

323   thickness of layer i, and C_l represents the variable at the lowest layer in the model. f_{conv} is the

324   weighting factor for the nonlocal and local effects (i.e., $f_{conv} = \frac{K_h\gamma_h}{K_h\gamma_h - K_h\frac{\partial \theta}{\partial z}}$), where the value of f_{conv}

325   ranges from 0 to 1, a larger f_{conv} indicates stronger nonlocal mixing.

326   There are two methods to calculate the TDC, and the first method is the same as the YSU scheme,

327   i.e., Eq. (3), but there is also a very stable condition in the ACM2 scheme. In this case, the

328   dimensionless function can be expressed as $\phi_m = \phi_h = \left(5 + \frac{0.1h}{L}\right)$.

329   The second calculation principle is based on the mixing length theory, which uses mixing length

330   and stability function to calculate TDC:

331     $K_h = 0.01 + l^2\sqrt{ss}f_h(Ri)$ (11)

332   where l is similar to the MYJ scheme, but l_0 is a constant (=80), ss is the wind shear ($ss =$

333     $(\partial \overline{u}/\partial z)^2 + (\partial \overline{v}/\partial z)^2$)), 0.01 denotes the minimum value of the TDC in the model, and $f_h(Ri)$ is

334   the empirical stability functions of gradient Richardson number of heat.

335   i.   when $Ri \geq 0$:

336     $f_h(Ri) = (1 - 25Ri)^{1/2}$ (12a)

337   ii.   when $Ri < 0$:

338     $f_h(Ri) = \frac{1}{1 + 10Ri + 50Ri^2 + 5000Ri^4} + 0.0012$ (12b)

339   Similarly, the empirical stability functions of momentum can be indicated as:

340   i.   when $Ri \geq \leftarrow 0$:

341   ~~i.~~   ~~$K_m = Pr \cdot K_h$ (13a)~~

342 ~~$f_m(Ri) = Pr \cdot f_h(Ri) + 0.00104$ (13a)~~

343 ~~$K_m = 0.01 + l^2\sqrt{ss}f_m(Ri)$ (13b)~~

344   ~~ii.~~   when $Ri < \geq 0$:

345 ~~$K_m = Pr \cdot K_h$ (13c)~~

346 $f_m(Ri) = Pr \cdot f_h(Ri) + 0.00104$ (13b)

347 $K_m = 0.01 + l^2\sqrt{ss}f_m(Ri)$ (13c)

348   The ACM2 scheme has a range setting for the TDC in the model with a minimum value of 0.01 m^2

349   s^{-2} and a maximum value that cannot exceed 1000 m^2 s^{-2}.

350   The PBLH discrimination in the ACM2 scheme is similar to the YSU scheme, and is defined with

351   the bulk Richardson number method. The difference is that the entrainment region at the top of the

352   PBL is considered in the ACM2 scheme, and turbulence still exists due to the wind shear and thermal

353   penetration. Therefore, special processing of the PBLH is required under unstable and stable

354   conditions.

355   **2.3.4 BL scheme**

356   The BL scheme is also a one-and-a-half order local closure scheme, and the TDC is calculated in a

357   similar way to Eq. (7) of the MYJ scheme. Nevertheless, the function S_m and mixing length (i.e., l)

358   are different from the MYJ scheme. In the BL scheme, S_m is a constant 0.4 and the l is divided into

359   upward and downward mixing length (i.e., l_{up} and l_{down}), which are defined as:

360    $\int_z^{z+l_{up}} \beta[\theta(z) - \theta(z')]\, dz' = e(z)$ (14a)

361    $\int_{z-l_{down}}^z \beta[\theta(z') - \theta(z)]\, dz' = e(z)$ (14b)

362   where, β is the buoyancy coefficient and the l is equal to the minimum of l_{up} and l_{down} (i.e., $l =$

363    $min(l_{up}, l_{down})$). It is worth noting that in the BL scheme the TDC of heat is equal to the TDC of

364   momentum (i.e., $K_h = K_m$). In addition, the PBLH of the BL scheme is defined as the height at which

365   the virtual potential temperature of a layer is greater than that of the first layer by 0.5 K.

366   To accommodate different methods of calculating PBLH for different schemes and to evaluate the

367   simulation performance of PBLH, two methods are employed to calculated PBLH using observed

368   data in this study, the first being the bulk Richardson number method, and the detailed calculation

369   principle is as follows (Miao et al., 2018):

370    $Ri(z) = \frac{(g/\theta_s)(\theta_z - \theta_s)(z - z_s)}{(u_z - u_s)^2 + (v_z - v_s)^2 + bu_*^2}$ (15)

371   here z is the height, g is the gravity, θ is the virtual potential temperature, u and v are the components

372   of the horizontal wind, b is a constant, and u_* is the friction velocity. The subscript "s" indicates

373 the near-surface. Since the friction velocity is much smaller in magnitude than the wind shear, the

374 b is set to 0, ignoring the effect of surface friction (Vogelezang and Holtslag, 1996; Seidel et al.,

375 2012). The PBLH is estimated as the lowest layer height when Ri reaches a critical value of 0.25.

376 The second method adopts the same calculation method as the BL scheme, i.e., the virtual potential

377 temperature method:

378 $\Delta \theta_{v|PBLH} = \theta_{v1} + 0.5$ (16)

379 The PBLH is the height when the virtual potential temperature exceeds the virtual potential

380 temperature of the first level by 0.5 K.

381 **2.4 Evaluation of the model**

382 To evaluate the PBL schemes and the performance of the model for estimating meteorological

383 variables, the statistical parameters used in this statistical analysis are defined as follows(Emery et

384 al., 2017):

385 Index of agreement (IOA):

386 $IOA = 1 - \dfrac{\left[\sum_{i=1}^{n} |X_{sim,i} - X_{obs,i}|^2\right]}{\left[\sum_{i=1}^{n}(|X_{sim,i} - \overline{X_{obs}}| + |X_{obs,i} - \overline{X_{obs}}|)^2\right]}$ (17)

387 Mean bias (MB):

388 $MB = \dfrac{1}{n}\sum_{i=1}^{n}(X_{sim,i} - X_{obs,i})$ (18)

389 Root mean square error (RMSE):

390 $RMSE = \sqrt{\dfrac{1}{n}\sum_{i=1}^{n}(X_{sim,i} - X_{obs,i})^2}$ (19)

391 Normalized standard deviations (NSD):

392 $NSD = \dfrac{\sqrt{\dfrac{1}{n-1}\sum_{i=1}^{n}(X_{sim,i} - \overline{X_{sim}})^2}}{\sqrt{\dfrac{1}{n-1}\sum_{i=1}^{n}(X_{obs,i} - \overline{X_{obs}})^2}}$ (20)

393 Relative bias (RB):

394 $RB = \dfrac{\overline{X_{sim}} - \overline{X_{obs}}}{\overline{X_{obs}}} \times 100\%$ (21)

395 Where $X_{sim,i}$ and $X_{sim,i}$ represent the value of simulation and observation, respectively, *i* refers

396 to time and *n* is the total number of time series. $\overline{X_{sim}}$ and $\overline{X_{obs}}$ represent the average simulation

397 and observation.

398 The Taylor diagram is a compact tool that displays simultaneously the values of four statistical

399 parameters: IOA, NSD, RB, and RMSE. In particular, in these diagrams the perfect match of a

400 model with the observations would be the point with IOA=1, NSD=1, RB=0 and RMSE=0.

401 **3 Results and discussion**

402 In section 3.1, the mechanistic analysis of the PBL schemes for the simulation of near-surface

403 meteorological parameters, including 2-m temperature, 2-m relative humidity, 10-m wind speed and
404 direction. Section 3.2 gives an in-depth analysis of different schemes for PBL vertical structures. In
405 section 3.3, the PBLH was evaluated for different schemes. In section 3.4, the reason for the
406 differences in turbulent diffusion are interrogated from the calculation principle of the schemes.
407 Section 3.5 summarizes the performance and expressiveness of different PBL schemes in different
408 regions, and recommends the optimal choice of PBL scheme.

409 **3.1 surface meteorological variables**

410 **3.1.1 2-m temperature and relative humidity**

411 To better analyze the variation of the time series, we selected representative stations in different
412 regions. Figure 2 shows the diurnal variation of 2-m temperature (i.e., T_2) for four months (i.e.,
413 January, April, July and October 2016) at representative sites (indicated in the ~~orange~~ purple dots in
414 Fig. 1) in the five regions. The model basically captures the daily variation characteristics of T_2, but
415 there are significant differences between different regions and seasons. The simulated results for
416 July are closest to the observed values (Fig. 2 c1-c5), anywhere. Overall, the mean biases (MBs) of
417 the diurnal variation of T_2 predicted in July for the NCP, YRD, SB, PRD and NS regions are
418 0.61~1.19, -0.02~-0.56, -0.32~-0.60, -0.38~-0.69, and 0.28~0.81 ℃, respectively. However, a
419 smaller value of the mean bias does not mean that the simulated value of the model is closer to the
420 observed value. For example, if one overestimation and the other underestimation occur during the
421 day and night, the average results will cancel each other out, resulting in a small mean bias.
422 Accordingly, more statistical parameters are needed to further evaluate the optimal scheme. In the
423 other three months (January, April, and October), the simulated results of T_2 are overestimated to
424 varying degrees during daytime in the YRD, SB and PRD regions, while in the NS region, T_2 are
425 underestimated to varying degrees (Fig. 2 a2-b5, d2-d5 and Table 1). In the NCP regions, T_2 presents
426 underestimation in January by the model with the YSU, ACM2, BL and MYJ schemes are -1.33, -
427 1.21, -0.52 and -1.18 ℃, respectively, while overestimation arises in the other three months (Table
428 1). In the five regions, the simulation results of the nighttime T_2 outperform those of the daytime T_2
429 for almost four months. At night, the MYJ scheme shows a significant underestimation of T_2 for all
430 months in five regions compared to the other three schemes (Fig. 2 and Table 1). The simulation
431 results of Hu et al. (2010) and Xie et al. (2012) have also obtained the lowest temperature for the
432 MYJ scheme during the nighttime.
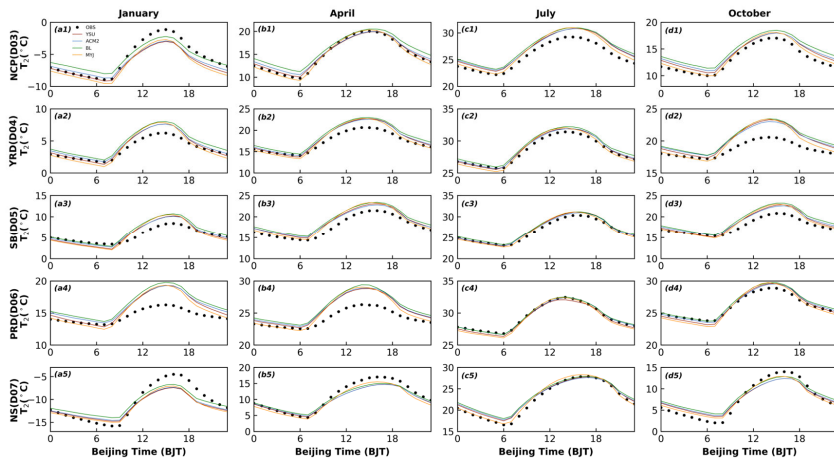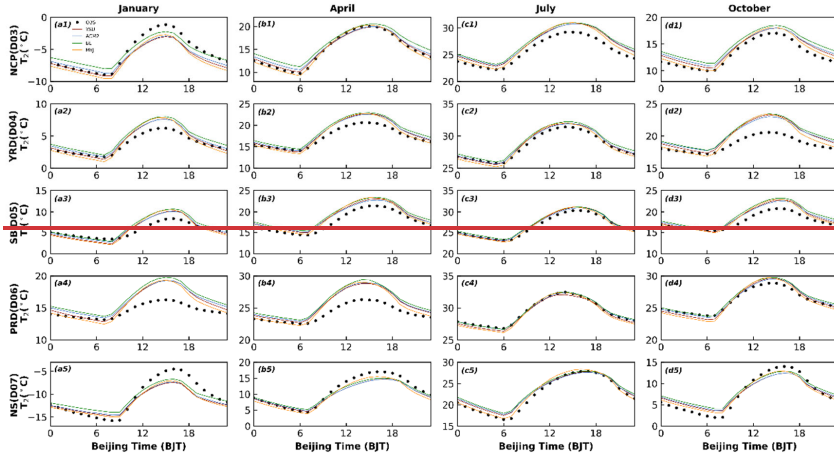
433

434

435 **Figure 2. Time series of diurnal variation of observed and simulated 2-m temperature in five**

436 **regions for four seasons.**

437 The 2-m temperature does not actually represent the air temperature at a height of 2 m, but it is a

438 diagnostic variable of the near-surface temperature. It is calculated from the surface temperature

439 (T_s), the sensible heat flux (HFX) and the heat transfer coefficient (C_h). The T_s is a prognostic

440 variable, which is obtained in the model through the energy balance equation:

441 $(1-\alpha)S\downarrow +L\downarrow -L\uparrow +G - HFX - LH = 0$ (22)

442 where α is the albedo of the underlying surface, $S\downarrow$ represents the downward of the shortwave

443 radiation, $L\downarrow$ is the downward of the longwave radiation emitted by the cloud and atmosphere,

444 $L\uparrow$ is the upward of the longwave emitted by the ground surface, G is the ground heat flux, and it

445 is positive when heat transfers from the soil to the near surface, HFX is the sensible heat flux and

446 LH is the latent heat flux.

447 We compare the effects of the six variables mentioned above on T_s with the expectation that we can

448 further examine the reasons for the differences in T_2 variation between different schemes. The YSU

449 scheme is used as a control and analyzed in comparison with each of the schemes.

450 The nonlocal closure scheme (YSU) and the local closure scheme (MYJ) are compared first.

451 Theoretically, the greater the downward shortwave radiation ($S\downarrow$) becomes, the more energy reaches

452 the ground, and the higher the surface temperature (T_s) is. After comparing the YSU and MYJ

453 schemes, the surface temperature does not show a proportional change with the downward

454 shortwave radiation, and the $S\downarrow$ of the MYJ scheme is almost the same as that of the YSU scheme

455 (Fig. 3 a1-e1), but the T_s of the MYJ scheme is the lowest (Fig. 4 a1-e1). Therefore, the $S\downarrow$ is not

456 the main factor that causes the difference in T_s between the two schemes. There is no significant

457 difference in the upward/downward longwave radiation between these two schemes (Fig. 3 a2-e3),

458 so the effect of longwave radiation on the T_s can also be excluded. During the daytime, the MYJ

459 scheme transfers less heat from the surface to the soil than the YSU scheme (Fig. 3 a4-e4), and the

460 T_s of the MYJ scheme should be higher than that of the YSU scheme. But that's not how it has

461 turned out (Fig. 4 a1-e1). Thus, the ground heat flux (G) is also not a key factor that directly affects

462 the T_s. The latent heat flux (LH) is mainly related to water vapor (or relative humidity), so further

463 attention is paid to the effect of sensible heat flux (HFX) on T_s (Fig. 3 a5-e6). The HFX is determined

464 by the difference between the surface temperature and the 2-m temperature (T_s-T_2), and the heat

465 transfer coefficient (C_h) $(HFX = \rho C_h u_1(T_s - T_2)$, here, ρ is the air density, u_1 is the wind

466 speed at the first level of the model). MYJ has the largest HFX, and transfers more heat from the

467 surface to the atmosphere, resulting in the largest energy loss at the surface, which should

468 correspond to the smallest T_s (Fig. 3 a6-e6, 4 a1-e1). The smallest difference between the two

469 temperatures indicates a smaller temperature gradient and more uniform mixing, symbolizing the

470 largest C_h, which is also true (Fig. 4 a2-e3). A larger C_h would lead to higher T_2 during the day.

471 Although the T_s of the MYJ scheme is significantly lower than YSU scheme, it makes the T_2 higher

472 due to the large C_h. During the daytime, the less heat is transferred from the surface to the soil in

473 the MYJ scheme, which results in lower soil temperature. During the nighttime, the difference in

474 HFX and temperature gradient between the two schemes decreases, and the lower soil temperature

475 results in lower T_s and T_2.
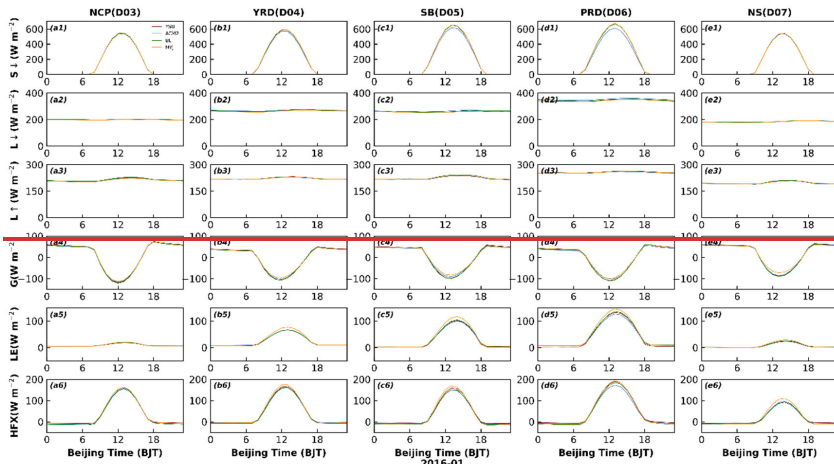
476
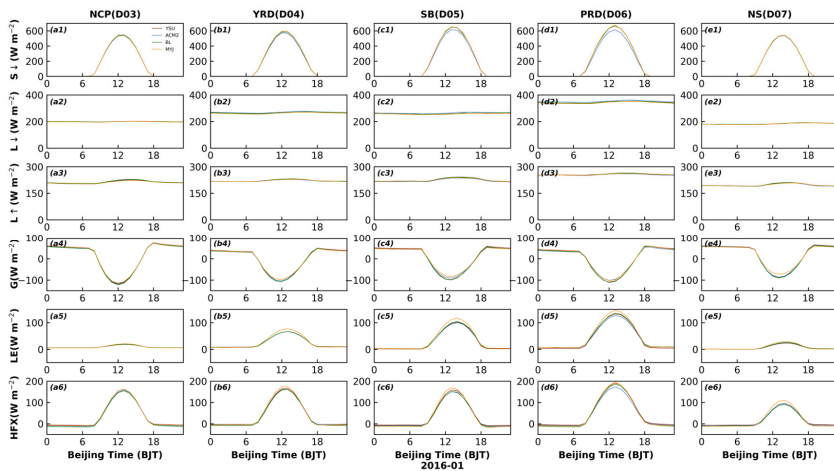
477

478 **Figure 3. Time series of diurnal variation of (a1-e1) downward shortwave radiation (S ↓), (a2-e2)**

479 **downward longwave radiation (*L* ↓), (a3-e3) upward longwave radiation (*L* ↑), (a4-e4) ground heat**

480 **flux (G), (a5-e5) latent heat flux (LH), and (a6-e6) sensible heat flux (HFX) by four PBL schemes**

481 **in five regions in January.**

482 The differences between the YSU scheme and the ACM2 scheme are further explored. Except for

483 the NCP and NS regions, the **S** ↓ of the ACM2 scheme is smaller than that of the YSU scheme in

484 the other three regions (i.e., YRD, SB and PRD) (Fig. 3 b1-d1). The HFX of the ACM2 scheme is

485 smaller than that of the YSU scheme (Fig. 3 b6-d6), the heat loss from the surface of the ACM2

486 scheme is less, and the T_s of the ACM2 scheme should be higher. However, the T_s corresponding to

487 the ACM2 scheme is lower than that of the YSU scheme (Fig. 4 b1-d1), reflecting that the **S** ↓

488 varies proportionally with the T_s, and it is the main factor controlling the T_s variation. In the ideal

489 case, assuming the same temperature gradient for the nonlocal schemes, the T_2 of the YSU scheme

490 should also be higher than that of the ACM2 scheme when the T_s of the YSU scheme is higher than

491 that of the ACM2 scheme with the same C_h. But in fact, it can be seen that the C_h of the ACM2

492 scheme and YSU scheme are the same (Fig. 4 b2-d2), and the temperature gradient of the YSU

493 scheme is greater than that of ACM2 scheme (Fig. 4 b3-d3). The T_2 of the ACM2 scheme should be

494 slightly higher than the ideal case, closer to the T_2 of the YSU scheme, and even may also exceed

495 T_2 of the YSU scheme. At night, the T_s of the YSU scheme is lower than that of the ACM2 scheme,

496 and the C_h of the YSU scheme is smaller than that of the ACM2 scheme (Fig. 4 a1-e2). Meanwhile,

497 the difference in HFX between the two schemes is not obvious at night, contributing to lower T_2 of

498 the YSU scheme. In both NCP and NS regions, there is no significant difference in downward

499 shortwave radiation between two schemes, and no noticeable difference between T_2 and T_s.
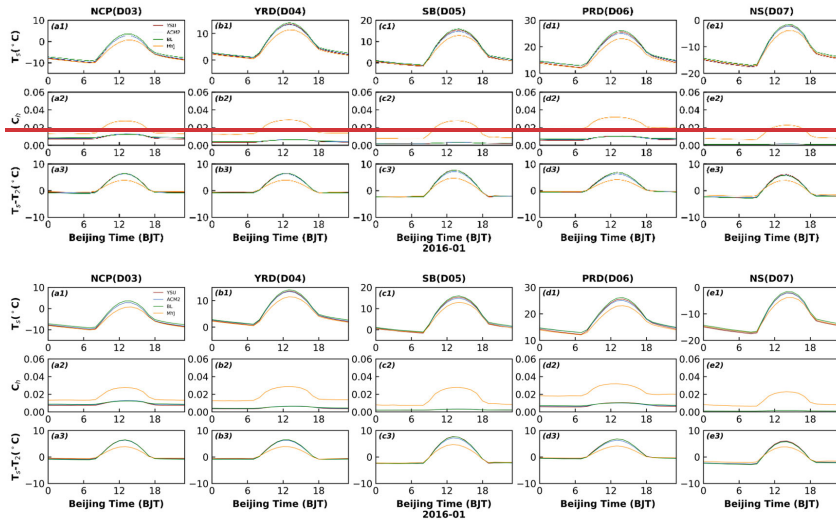
500

501

502 **Figure 4. Time series of diurnal variation of (a1-e1) surface temperature (T_s), (a2-e2) heat transfer**

503 **coefficient (C_h) and (a3-e3) the difference between the surface temperature and the 2-m**

504 **temperature (T_s-T_2) by four PBL schemes in five regions in January (Winter).**

505 Then, the reasons for the simulated temperature difference between the YSU scheme and the BL

506 scheme are demonstrated. During the daytime, the $S\downarrow$ of both schemes are the same (Fig. 3 a1-e1),

507 but the HFX of the BL scheme is smaller than that of the YSU scheme (Fig. 3 a6-e6), less heat is

508 loss at the surface, hence the T_s should be higher than that of the YSU scheme (Fig. 4 a1-e1). The

509 C_h of both schemes are the same, thus, the BL scheme has a higher T_2 (Fig. 2, 4a1-e2). At night, the

510 HFX of BL scheme is larger than that of YSU scheme, and more heat is transferred from atmosphere

511 to the surface, and the larger C_h resulting in higher T_2 (Fig. 3 a6-e6, 4 a1-e2).

512 Finally, we can also uncover the reasons for the difference between the local closure schemes (MYJ
513 and BL). The larger HFX of the MYJ scheme leads to a lower T_s in the daytime, while the
514 temperature gradient of MYJ scheme is smaller than that of the BL scheme, and C_h is larger than
515 BL scheme (Fig. 3 a6-e6, 4). Therefore, the difference in T_2 between the two schemes is smaller
516 than that in T_s. The T_2 of the MYJ scheme is closer to that of the BL scheme.

517 In conclusion, the causes of temperature differences simulated by the nonlocal closure schemes
518 should first focus on the effect of the downward shortwave radiation ($S\downarrow$), and when it comes to the
519 local closure scheme, the effect of HFX should be further concerned. All of the above results have
520 been analyzed for January 2016, and the results for the other three months are similar (Figs. S1-S6).
521 The results for the months of January, April and October differ slightly from those of July. In terms
522 of regional distribution differences, T_2 in the northern and near mountainous regions of the NCP
523 region is significantly underestimated in the daytime for January, April and October, while T_2 in
524 other areas of the NCP region regions shows an overestimation (Fig. 5, S7, S8 a1-e1). The range of
525 overestimated areas is smaller than the underestimated in January, only in a small part of the area
526 south of Hebei and Shandong pProvinces (Fig. 5 a1-e1). The relative bias (RB) of the
527 underestimated (overestimated) T_2 with the YSU, ACM2, BL and MYJ schemes are -0.60% (0.15%),
528 -0.57% (0.17%), -0.43% (0.26%) and -0.60% (0.20%), respectively in January. Also in these three
529 months, temperature is overestimated at almost all stations in the YRD region (RB=0.38%~0.50%
530 in January, RB=0.49%~0.65% in April and RB=0.58%~0.70% in October) and underestimated at
531 some stations along the coast (RB=-0.13%~-0.24% in January, RB=-0.32%~-0.37% in April and
532 RB=-0.23%~-0.28% in October) (Fig. 5, S7, S8 a2-e2). The results show an overestimation of T_2
533 simulated in those stations in the basin for the SB region as well as the simulation results of the
534 stations in the plain for the NCP region, while for the stations in the hilltop areas, the T_2 shows an
535 underestimation (Fig. 5, S7, S8 a3-e3). In the PRD region, the entire region exhibits an
536 overestimation of T_2, with the simulation results in October (RB=0.06%~0.15%) being significantly
537 better than those in January (RB=0.59%~0.81%) and April (RB=0.56%~0.67%), with a lower
538 degree of T_2 overestimation (Fig. 5, S7, S8 a4-e4). The BL scheme simulates a higher T_2 and a large
539 range of overestimated areas (about 167, 378, 252 and 100 stations in NCP, YRD, SB and PRD
540 regions). The NS region has a more complex topography and higher elevation, and the T_2 is
541 underestimated at almost all stations, with best simulation results in October (RB=-0.04%~-0.21%)
542 and worst in April (RB=-0.49%~-0.64%).

543 For July, when the temperature is higher, the simulation results are significantly different from the
544 other three months. The relative bias of T_2 simulated with the YSU, ACM2, BL and MYJ schemes
545 are 0.47%, 0.46%, 0.53% and 0.46%, respectively, in the NCP region. The overestimation results
546 are similar to daytime, with the most pronounced overestimation for the BL scheme. For the
547 southern region of the NCP, the T_2 is consistently overestimated regardless of the season (Fig. S9

a1-e1). The T_2 at most stations are underestimated in the YRD region, which is different form the other three months (Fig. S9 a2-e2). In summer, the temperature of the ocean, affected by the subtropical high (prevailing southeasterly winds), is lower than that of the land, and the transport of momentum is accompanied by the transport of heat from the sea to the land, causing the temperature of the land to decrease. The T_2 of the basin area in the SB region is well reproduced, and no significant overestimation occurs (Fig. S9 a3-e3). There is an underestimation of the T_2 at most stations in the PRD region, but to a lesser extent (Fig. S9 a4-e4). In contrast, for the NS region, the temperature is overestimated for areas at lower elevations, while underestimated (or better reproduced) for areas at higher elevations (Fig. S9 a5-e5).
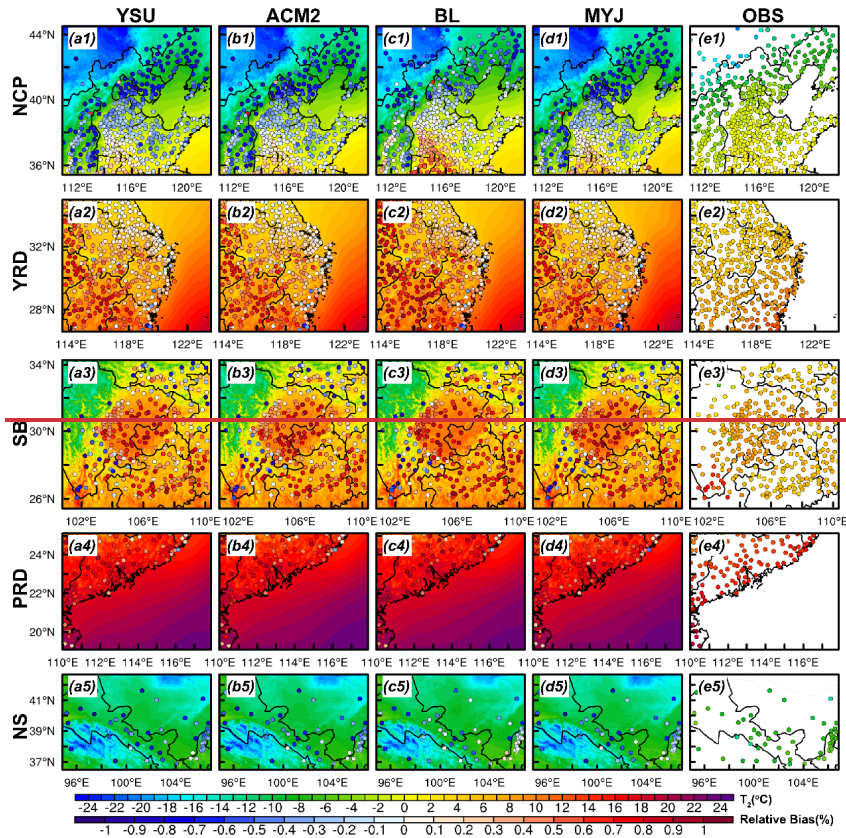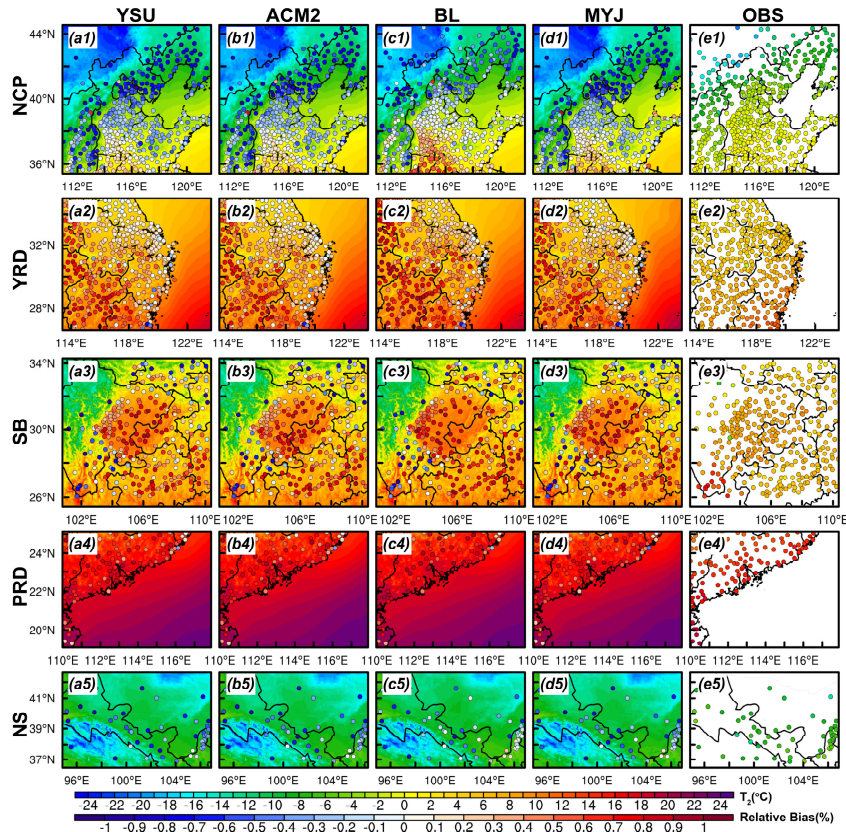
Figure 5. Regional distribution of 2-m temperature simulated by (a-d) four PBL schemes in five regions during the daytime in January (Winter), (e1-e5) distribution of observation in five regions, and (a1-d5) distribution of relative bias between simulations and observations is denoted by scatters.

The relative deviation of the nighttime T_2 simulations is less than that of the daytime, regardless of the region and month (Fig. 6, S10-S12). The differences between the four schemes are more striking at night compared to the daytime. The BL scheme simulates the highest T_2 and the MYJ scheme simulates the lowest T_2 in the whole region (Fig. 6, S10-S12). Compared to the observed values, the MYJ scheme is the best when all schemes overestimate the simulated temperature, but if there is an underestimation, the MYJ scheme is no longer the best scheme. Later, a comprehensive statistical evaluation of the schemes will be presented. For the NCP region, the overestimation and underestimation in the whole region do not show a north-south divide (or a mountain-plain divide) as in the daytime (Fig. 5, 6 a1-e1). In the YRD region, the temperature along the coastal area still shows a significant underestimation (Fig. 6, S10-S12 a2-e2). Similar to the daytime, the temperature

573 at stations in the hill top areas of the SB region still presents an underestimation (Fig. 6, S10-S12
574 a3-e3). Most stations show the underestimation of T_2 in July and October in the PRD region (Fig.
575 S11-S12 a4-e4). In the NS region, the relative deviation of temperature simulations in October is
576 greater than that in daytime (RB=0.17%~0.56%) (Fig. 5, S12 a5-e5).

577
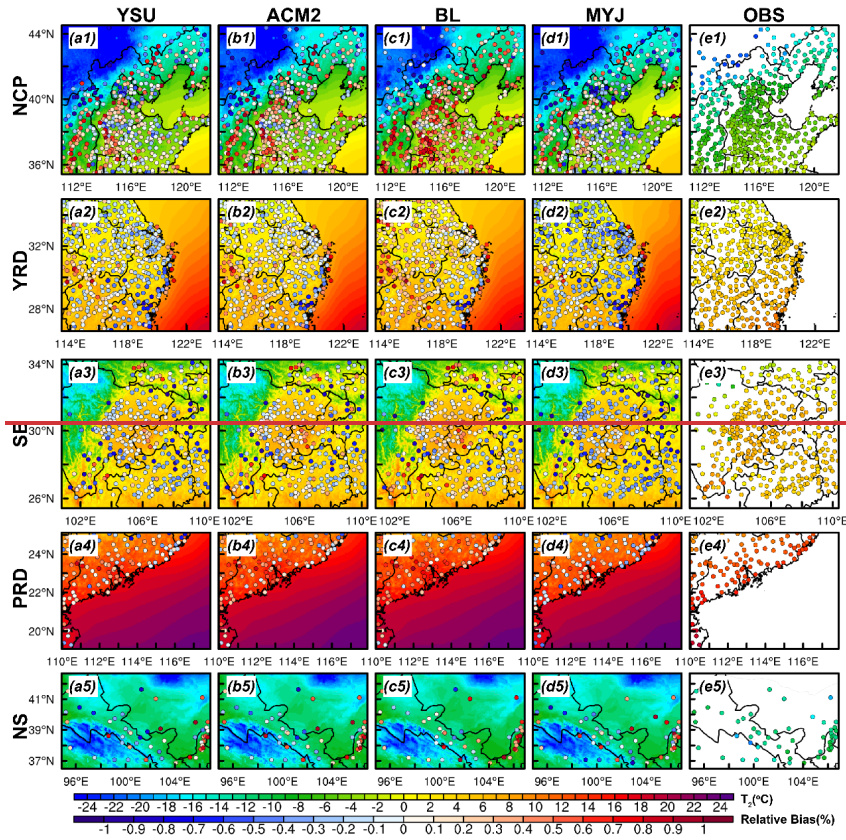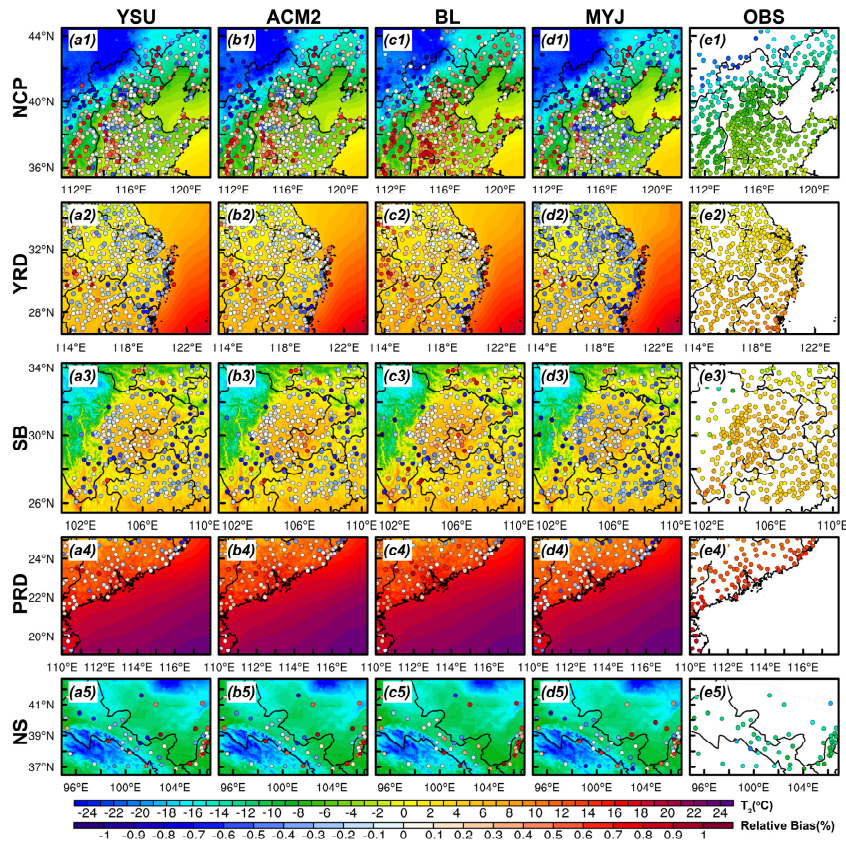
Figure 6. Similar as ~~f~~Figure 5, but at night.

In summary, the simulation results of T_2 have the following main characteristics. From the perspective of differences between observations and simulations, (1) the simulation results for July are better compared to the other three months. (2) The simulation results at night are better than those at daytime, with less relative deviation, especially in winter (i.e., January and October). (3) The temperature is easily underestimated at higher altitudes while overestimated in plains and basin areas. From the perspective of the differences between the different schemes, (1) the differences in the performance of the four schemes are more noticeable at night. (2) The difference in the simulation of temperature in the nonlocal closure schemes is mainly attributed to the difference in downward shortwave radiation ($S \downarrow$), and the difference in the variation of sensible heat flux (HFX) needs to be further analyzed when the local closure schemes are involved. (3) The BL scheme simulates the highest temperature and the MYJ scheme for the lowest temperature.

The results for 2-m relative humidity (RH_2) and T_2 correspond to each other, and the overestimation of T_2 corresponds to the underestimation of RH_2. The simulation of RH_2 still shows the best results

593 in July, with the highest simulated values for the MYJ scheme and the lowest for the BL scheme.

594 Except for the NS region, the simulated RH_2 of the other four regions is almost underestimated.

595 This uniform trend in relative humidity may be due to errors in the initial field, which will be

596 discussed in Part II. Too much will not be repeated here (Figs. 2, 7).

597

598
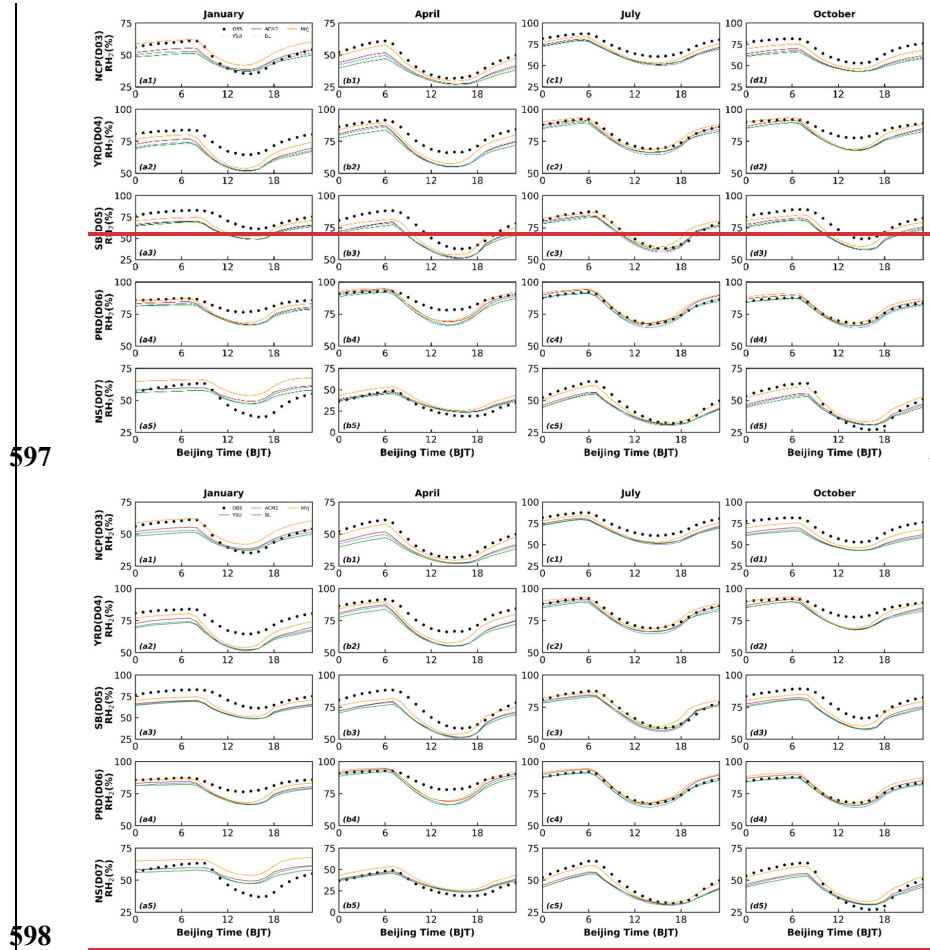
599 **Figure 7. Similar as fFigure 2, but for 2-m relative humidity.**

600 **3.1.2 10-m wind speed and direction**

601 Although the model simulates the diurnal cycle of wind speed, the wind speed shows different

602 degrees of overestimation, and the mean bias is in the range of 0.86 m s^{-1}~2.74 m s^{-1} (Fig. 8, Table

603 2). This is also the conclusion reached in many previous studies and it is more widely accepted by

604 the public(Cohen et al., 2015; Wenxing Jia and Zhang, 2020; W. Jia and Zhang, 2021; Jiménez and

605 Dudhia, 2012). Except for the NCP region where the MYJ scheme has the largest mean bias (MB)
606 value during the day (YSU: MB=1.6 m s^{-1}, ACM2: MB=1.8 m s^{-1}, BL: MB=1.7 m s^{-1}, MYJ: MB=2.1
607 m s^{-1}), while the BL scheme has the largest MB value at night regardless of the region (YSU:
608 MB=1.3 m s^{-1}, ACM2: MB=1.8 m s^{-1}, BL: MB=2.2 m s^{-1}, MYJ: MB=1.7 m s^{-1}) (Fig. 8, Table 2).
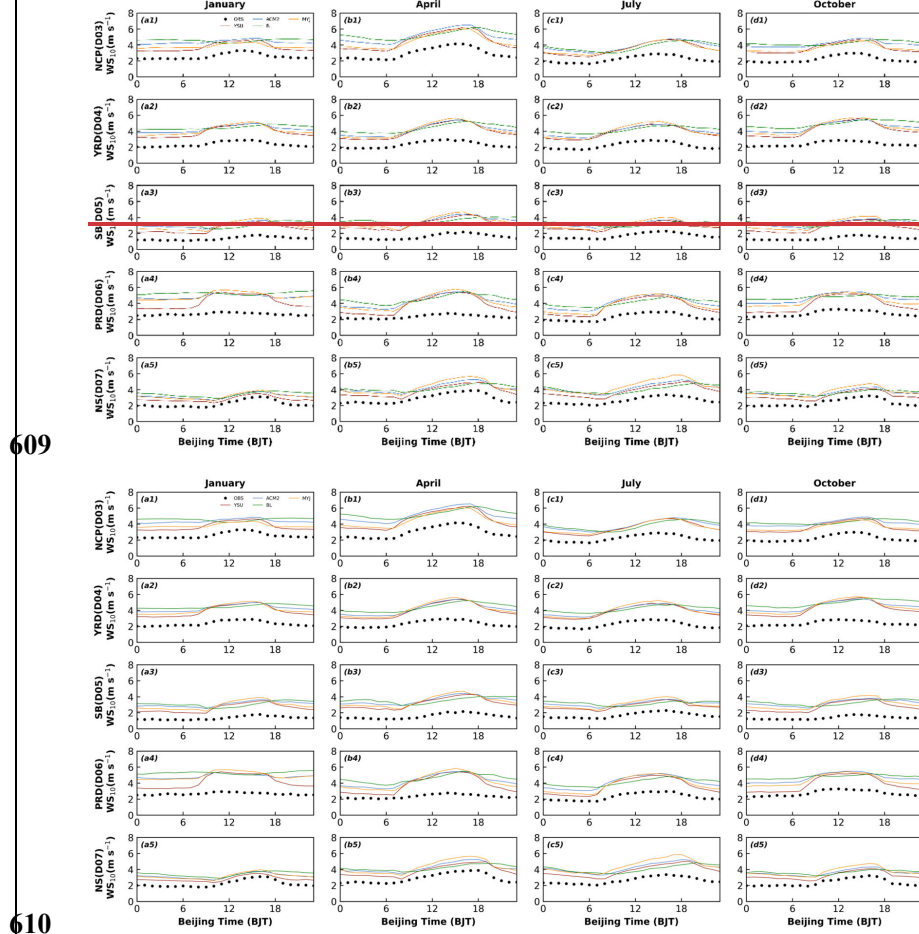
609
610
611 **Figure 8. Similar as ~~fF~~igure 2, but for 10-m wind speed.**

612 **Table 2. Mean bias of 2-m temperature, 2-m relative humidity and 10-m wind speed during daytime**
613 **and nighttime by four PBL schemes in five regions and four seasons.**

Variables	Schemes/Seasons	Regions	NCP	YRD	SB	PRD	NS
T$_2$-Day	YSU	Jan	-1.33	0.91	0.20	1.84	-1.42
		Apr	0.27	1.35	0.77	1.74	-1.83
		Jul	1.41	-0.18	-0.20	-0.66	0.38
		Oct	0.91	1.69	0.68	0.25	-0.58

	ACM2	Jan	-1.21	0.97	0.29	1.93	-1.29
		Apr	0.34	1.28	0.64	1.79	-1.82
		Jul	1.37	-0.21	-0.31	-0.49	0.27
		Oct	0.98	1.54	0.61	0.21	-0.50
	BL	Jan	-0.52	1.33	0.73	2.32	-0.76
		Apr	0.89	1.71	1.07	2.00	-1.43
		Jul	1.60	0.04	-0.16	-0.38	0.55
		Oct	1.49	1.88	1.09	0.46	-0.09
	MYJ	Jan	-1.18	0.92	0.32	1.70	-1.23
		Apr	0.45	1.19	0.87	1.66	-1.39
		Jul	1.38	-0.29	-0.28	-0.58	0.64
		Oct	0.83	1.56	0.68	0.18	-0.45
T_2-Night	YSU	Jan	-0.14	-0.27	-0.98	0.15	0.33
		Apr	0.04	-0.17	0.13	0.24	-0.23
		Jul	0.39	-0.53	-0.78	-0.54	0.68
		Oct	0.51	0.06	-0.52	-0.56	1.04
	ACM2	Jan	0.15	0.03	-0.74	0.56	0.52
		Apr	0.47	0.07	0.23	0.39	-0.07
		Jul	0.57	-0.40	-0.72	-0.27	0.86
		Oct	0.86	0.35	-0.29	-0.28	1.24
	BL	Jan	0.88	0.34	-0.45	0.80	1.03
		Apr	1.21	0.48	0.53	0.64	0.23
		Jul	0.79	-0.08	-0.48	-0.21	1.07
		Oct	1.37	0.54	-0.06	-0.04	1.59
	MYJ	Jan	-0.46	-0.59	-1.16	-0.28	0.21
		Apr	-0.70	-0.62	-0.27	-0.19	-0.97
		Jul	-0.15	-0.83	-0.93	-0.80	-0.08
		Oct	0.01	-0.34	-0.74	-0.83	0.52
RH_2-Day	YSU	Jan	-0.01	-9.95	-10.71	-6.62	7.19
		Apr	-7.09	-7.59	-5.75	-5.02	3.02
		Jul	-8.46	1.18	-0.16	3.18	-5.56
		Oct	-11.07	-5.62	-5.17	0.57	-1.02
	ACM2	Jan	-0.92	-10.77	-11.63	-7.43	6.05
		Apr	-7.82	-8.32	-6.64	-7.12	2.03
		Jul	-9.79	-0.65	-1.71	0.51	-6.18
		Oct	-11.83	-5.93	-6.23	-1.44	-2.09
	BL	Jan	-1.66	-10.53	-11.36	-7.54	5.40
		Apr	-7.89	-8.32	-5.90	-6.31	2.36
		Jul	-8.02	0.68	0.92	1.71	-5.06
		Oct	-12.47	-6.10	-5.67	-0.38	-2.10
	MYJ	Jan	4.47	-6.72	-7.69	-4.74	12.55
		Apr	-4.39	-4.26	-3.08	-3.59	5.59
		Jul	-5.59	3.85	3.31	4.22	-3.01
		Oct	-7.44	-3.55	-2.61	2.47	2.72
RH_2-Night	YSU	Jan	-5.11	-7.90	-10.62	-3.29	-0.03
		Apr	-9.65	-5.01	-6.63	0.47	-0.14
		Jul	-5.50	1.09	-1.33	2.48	-6.95
		Oct	-12.34	-1.44	-4.83	1.62	-7.79
	ACM2	Jan	-6.38	-9.54	-11.03	-4.56	-0.48
		Apr	-11.35	-5.91	-7.05	-0.86	-1.15
		Jul	-6.86	-0.64	-2.25	0.18	-7.96
		Oct	-14.11	-2.92	-5.69	-0.94	-8.85
	BL	Jan	-8.40	-10.47	-11.89	-5.01	-2.36
		Apr	-13.51	-8.00	-8.25	-2.07	-2.16
		Jul	-7.32	-1.75	-2.47	-0.23	-8.06
		Oct	-15.92	-3.51	-6.19	-0.91	-9.94
	MYJ	Jan	1.84	-3.86	-6.91	-0.69	6.86
		Apr	-3.89	-1.65	-3.44	1.91	5.84

		Jul	-1.68	3.02	0.42	3.61	-1.91
		Oct	-7.18	1.04	-2.50	3.36	-1.45
WS$_{10}$-Day	YSU	Jan	1.33	1.92	1.58	2.17	0.59
		Apr	1.86	1.97	2.04	2.25	0.93
		Jul	1.35	1.56	1.20	1.79	1.30
		Oct	1.68	2.11	1.54	1.70	0.93
	ACM2	Jan	1.57	2.04	1.79	2.26	0.91
		Apr	2.11	2.01	2.18	2.37	1.21
		Jul	1.43	1.62	1.30	2.02	1.50
		Oct	1.90	2.19	1.73	2.05	1.21
	BL	Jan	1.50	2.02	1.63	2.40	1.01
		Apr	1.85	2.04	1.93	2.44	0.86
		Jul	1.21	1.54	1.12	1.72	1.10
		Oct	1.83	2.28	1.60	1.95	1.04
	MYJ	Jan	1.63	2.26	2.14	2.67	1.10
		Apr	2.33	2.40	2.65	2.69	1.61
		Jul	1.85	2.05	1.85	2.16	2.09
		Oct	2.01	2.58	2.17	2.12	1.55
WS$_{10}$-Night	YSU	Jan	1.26	1.43	1.50	1.40	0.88
		Apr	1.51	1.49	1.67	1.22	1.07
		Jul	1.16	1.32	1.15	1.16	1.07
		Oct	1.42	1.45	1.40	1.14	1.04
	ACM2	Jan	1.88	1.91	1.97	2.21	1.36
		Apr	2.15	1.81	2.07	1.79	1.53
		Jul	1.56	1.62	1.50	1.71	1.59
		Oct	1.98	1.92	1.80	1.98	1.59
	BL	Jan	2.32	2.32	2.13	2.74	1.63
		Apr	2.72	2.28	2.38	2.33	1.73
		Jul	1.79	2.09	1.75	2.08	1.71
		Oct	2.38	2.44	2.06	2.38	1.78
	MYJ	Jan	1.63	1.76	1.94	2.18	1.45
		Apr	1.79	1.70	2.12	1.71	1.53
		Jul	1.42	1.56	1.52	1.42	1.66
		Oct	1.74	1.81	1.83	1.68	1.65

614

615 Similar to T$_2$, 10-m wind speed (i.e., WS$_{10}$) is also a diagnostic variable of the near-surface wind

616 speed. For the YSU, ACM2 and BL schemes, in the revised MM5 surface layer scheme, WS$_{10}$ is

617 calculated based on the Monin-Obukhov (M-O) similarity theory(Monin and Obukhov, 1954). The

618 dimensionless profile function of momentum is denoted as:

619 $\phi_m\left(\frac{z}{L}\right) = \frac{\kappa z}{u_*}\frac{\partial u}{\partial z}$ (23)

620 where κ is the von Karman constant, u_* is the friction velocity, z is the height, L is the Obukhov

621 length, integrating the Eq. (23) with respect to height z:

622 $du = \frac{u_*}{\kappa}\left[\frac{dz}{z} - \frac{1-\phi_m\left(\frac{z}{L}\right)}{\frac{z}{L}}d\left(\frac{z}{L}\right)\right]$ (24)

623 integrate Eq. (24):

624 $\int_0^u du = \frac{u_*}{\kappa}\left\{\int_{z_0}^z \frac{dz}{z} - \int_{\frac{z_0}{L}}^{\frac{z}{L}}\left[1 - \phi_m\left(\frac{z}{L}\right)\right]d\ln\left(\frac{z}{L}\right)\right\}$ (25)

625 here, let $\psi_m\left(\frac{z}{L}\right) = \int_0^{\frac{z}{L}}\left[1 - \phi_m\left(\frac{z}{L}\right)\right]d\ln\left(\frac{z}{L}\right)$, where $\psi_m\left(\frac{z}{L}\right)$ is the integrated similarity function

626 for momentum.

627 Therefore, Eq. (25) can be indicated as $u = \frac{u_*}{\kappa}\left[\ln\left(\frac{z}{z_0}\right) - \psi_m\left(\frac{z}{L}\right) + \psi_m\left(\frac{z_0}{L}\right)\right]$, where z_0 is the

628 roughness length.

629 Based on the bulk transfer method, the momentum flux can be represented as $\tau = \rho u_*^2 = \rho C_m u^2$,

630 where τ is the momentum flux, C_m is the bulk transfer coefficient for momentum:

631 $C_m = \frac{u_*^2}{u^2} = \frac{\kappa^2}{\left[\ln\left(\frac{z}{z_0}\right) - \psi_m\left(\frac{z}{L}\right) + \psi_m\left(\frac{z_0}{L}\right)\right]^2}$ (26)

632 Thus, the wind speed at 10 m divided by the wind speed at a certain height can be written as:

633 $u_{10} = \frac{u_*}{\kappa}\left[\ln\left(\frac{z}{z_0}\right) - \psi_m\left(\frac{z}{L}\right) + \psi_m\left(\frac{z_0}{L}\right)\right] \cdot \frac{\left[\ln\left(\frac{10}{z_0}\right) - \psi_m\left(\frac{10}{L}\right) + \psi_m\left(\frac{z_0}{L}\right)\right]}{\left[\ln\left(\frac{z}{z_0}\right) - \psi_m\left(\frac{z}{L}\right) + \psi_m\left(\frac{z_0}{L}\right)\right]} = \frac{u_*}{\kappa}\left[\ln\left(\frac{z}{z_0}\right) - \psi_m\left(\frac{z}{L}\right) +$

634 $\psi_m\left(\frac{z_0}{L}\right)\right] \cdot \left(\frac{C_m}{C_{m10}}\right)^{1/2}$ (27)

635 where C_{m10} is the transfer coefficient for momentum at 10 m height:

636 $C_{m10} = \frac{\kappa^2}{\left[\ln\left(\frac{10}{z_0}\right) - \psi_m\left(\frac{10}{L}\right) + \psi_m\left(\frac{z_0}{L}\right)\right]^2}$ (28)

637 Comparing the C_m of the three schemes (i.e., YSU, ACM2 and BL schemes) at night, C_m is the

638 largest for the BL scheme, the second largest for the ACM2 scheme, and the smallest for the YSU

639 scheme (Fig. 9). Correspondingly, the BL scheme simulates the largest WS_{10}, ACM2 the second

640 largest, and the YSU the smallest (Fig. 8). The larger C_m corresponds to the stronger mixing, which

641 transports more momentum from the upper to the lower layers, making WS_{10} increase. Therefore,

642 the bulk transfer coefficient C_m controls the variation of WS_{10} at night. During the daytime, the C_m

643 of the BL scheme is smaller than that of the other two schemes, and the corresponding WS_{10} decrease

644 (Fig. 8, 9). However, the difference among the three schemes is smaller in daytime than that in

645 nighttime. The reason why the results of C_m and WS_{10} differ with the same calculation method is

646 because of the vertical variation of heat and momentum within the boundary layer involved in the

647 calculation. This will correlate to the vertical diffusion coefficients within the boundary layer that

648 will be discussed further in a later section.

設置了格式: 下标
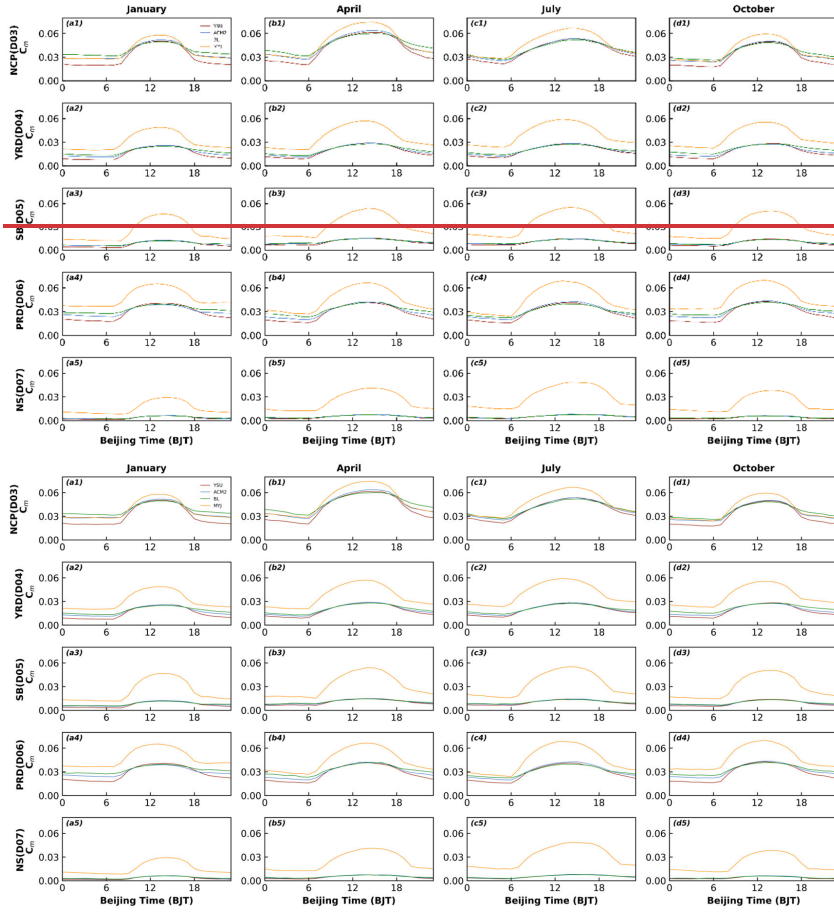
Figure 9. Similar as fFigure 2, but for momentum transfer coefficient (C_m).

For the near surface scheme of the MYJ scheme, WS_{10} is calculated according to the near surface

flux profile relationship proposed by Liu et al. (1979):

$$u_0 - u_s = D_1 \left[1 - exp\left(-\frac{z_u u_*}{D_1 \nu} \right) \right] \left(\frac{F_u}{u_*} \right) \quad (29)$$

where 0 represents the value at height z above the surface where the molecular diffusivity still plays

a dominant role, s denotes the surface value, D_1 denotes a near surface parameter, u_* is the friction

velocity, ν is the molecular diffusivity for momentum ($= 1 \times 10^{-5}$), and F_u is the momentum flux.

Since $1 - exp\left(-\frac{z_u u_*}{D_1 \nu} \right) \approx \frac{z_u u_*}{D_1 \nu}$, $u_0 - u_s = \left(\frac{z_u}{\nu} \right) F_u$.

The momentum flux in the surface layer above the viscous sublayer is represented by $F_u = $

$\left(\frac{C_m}{\Delta z_e} \right) (u_{low} - u_0)$, here, the subscript *low* denotes the variables at the lowest model level, Δz_e is

661 either the equivalent height of the lowest model level that considers the presence of the "dynamical

662 turbulence layer" at the bottom of the surface layer (Janjić, 1990). C_m is the bulk transfer coefficient,

663 defined as:

664 $$C_m = \frac{\kappa u_*}{\ln\left(\frac{z_0+z}{z_0}\right)+\psi_m\left(\frac{z_0+z}{L}\right)-\psi_m\left(\frac{z_0}{L}\right)} \quad (30)$$

665 In Eq. (29), z_u is still an unknown, such that $\frac{z_u u_*}{D_1 \nu} = \xi$, where ξ is a smaller constant (equal to

666 0.35 in the model). Here, the near surface parameter D_l is further defined as $D_1 = C \cdot$

667 $\left(\frac{z_0 u_*}{\nu}\right)^{1/4}$, where C is a constant (=30), the roughness length z_0 as a function of u_* ($z_0 = \frac{0.11\nu}{u_*} +$

668 $\frac{0.018u_*^2}{g}$), substituting D_l and z_u to Eq. (29):

669 $$u_0 = \frac{\frac{\xi}{u_*}\left[C\cdot\left(\frac{z_0 u_*}{\nu}\right)^{1/4}\right]\left(\frac{C_m}{\Delta z_e}\right)u_{low}+u_s}{1+\frac{\xi}{u_*}\left[C\cdot\left(\frac{z_0 u_*}{\nu}\right)^{1/4}\right]\left(\frac{C_m}{\Delta z_e}\right)} \quad (31)$$

670 The wind speed at a height of 10 m can be expressed as:

671 $$u_{10} = \frac{F_u \Delta z_e}{C_{m10}} + u_0 = \frac{C_m(u_{low}-u_0)}{C_{m10}} + u_0 \quad (32)$$

672 where C_{m10} is the transfer coefficient for momentum at 10 m height:

673 $$C_{m10} = \frac{\kappa u_*}{\ln\left(\frac{z_0+10}{z_0}\right)+\psi_m\left(\frac{z_0+10}{L}\right)-\psi_m\left(\frac{z_0}{L}\right)} \quad (33)$$

674 Therefore, the C_m of the MYJ scheme is significantly different from the other three schemes. Except

675 for the NCP region, although the C_m of the MYJ scheme is larger than the other three schemes at all

676 times of the day, the WS_{10} presents the maximum only during the daytime. This suggests that at

677 night, the wind speed simulated by the MYJ scheme also be influenced by other factors. For example,

678 the calculation method of the integrated similarity functions (ψ_m) in the MYJ scheme is different

679 from the other three schemes. In the other three schemes, the ψ_m is calculated according to four

680 stability regimes defined in terms of the bulk Richardson number(Zhang and Anthes, 1982). In the

681 MYJ scheme, the ψ_m is calculated based on two stability regimes by the z/L (Paulson, 1970).
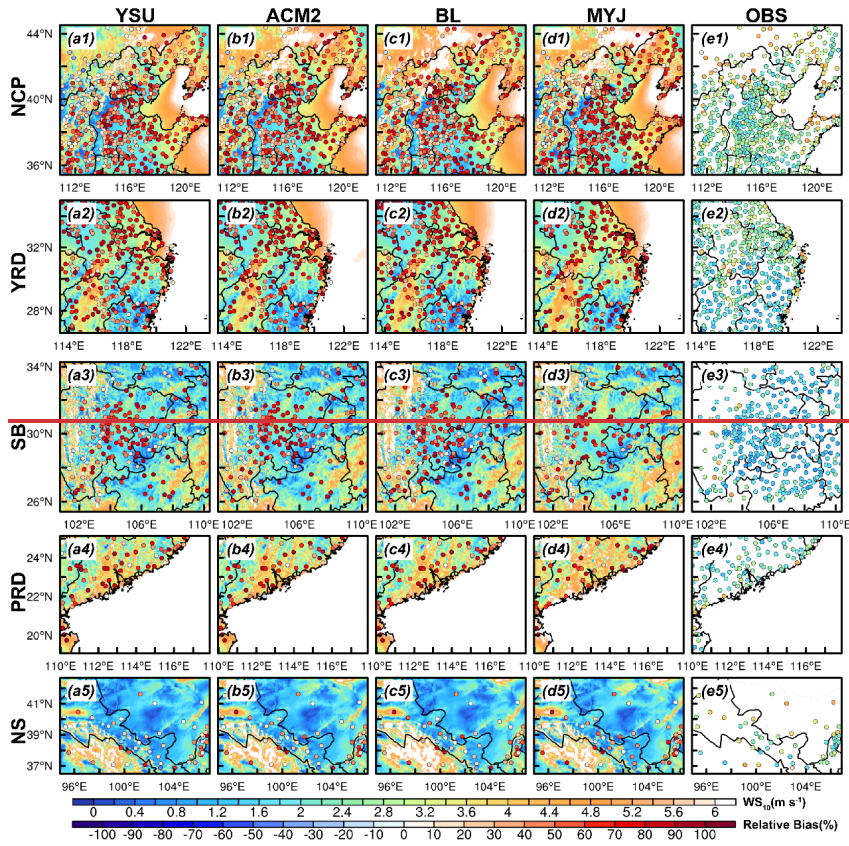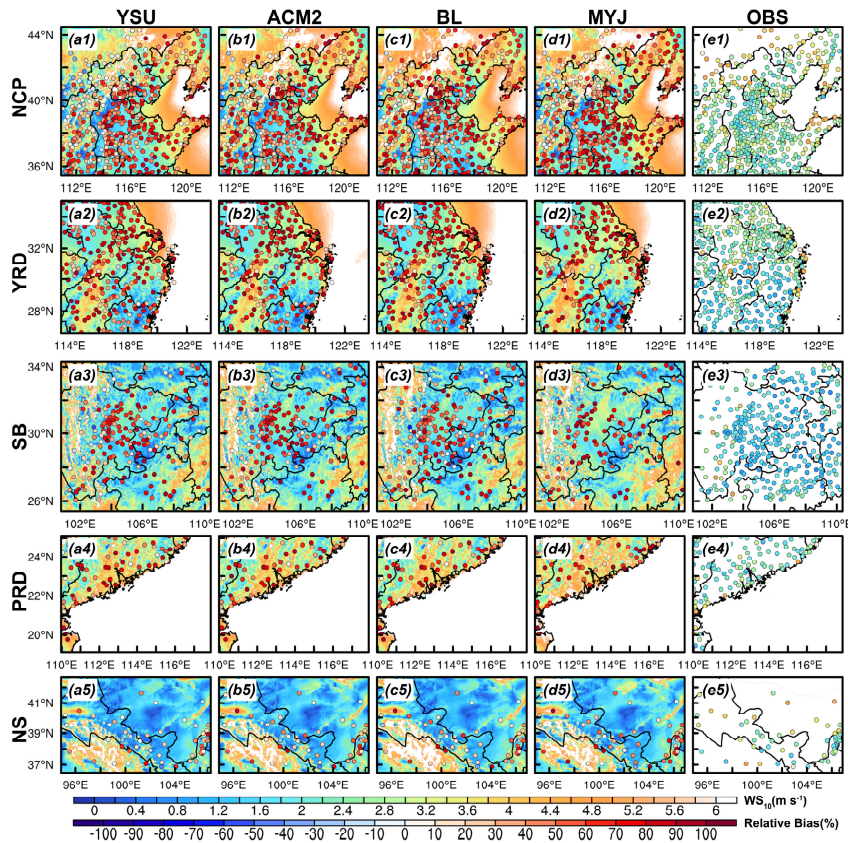
683

684 Figure 10. Similar as ~~f~~Figure 5, but for 10-m wind speed.

685 The reasons for the differences in WS_{10} simulation are further analyzed in terms of regional

686 distribution. During the daytime, wind speed is significantly overestimated at most sites throughout

687 the NCP region, which are centered in the plains and valleys, but is less overestimated and even

688 underestimated at some sites on the mountain tops (Fig. 10, S13-S15 a1-e1). Wind speed is

689 overestimated at almost all stations throughout the YRD and PRD regions (Fig. 10, S13-S15 a2-e2,

690 a4-e4). The WS_{10} in the basin is importantly overestimated in the SB region, while less

691 overestimated at hilltop stations on the eastern side of the basin, with higher wind speed being more

692 pronounced in January (Fig. 10, S13-S15 a3-e3). In the NS region, wind speed is overestimated to

693 a lesser extent than in other regions, but for regions with lower wind speed, the relative bias (RB)

694 is larger, especially in July (Jan: RB=29.3%~49.1%, Apr: RB=32.0%~55.6%, Jul:

695 RB=44.2%~78.7%, Oct: RB=42.7%~65.7%). Comparing the simulation results of the four schemes,

696 the MYJ scheme simulates the most significantly overestimated wind speed and the least

697 overestimated for the YSU scheme (Fig. 10, S13-S15). In comparison with the four months, it is

698 found that the RB of the simulation is the largest for the month with slower wind speed (i.e., July).
699 At night, the wind speed is overestimated at almost all stations in the whole region of NCP, and the
700 overestimation is greater at the hilltop stations than during the day (Fig. 11, S16-S18). The other
701 four regions are more similar to the daytime (Fig. 11, S16-S18). However, by comparing the four
702 schemes, we find that the BL scheme has the most obvious overestimation, different from the
703 daytime, while the YSU scheme still has the lowest overestimation, the same as the daytime. In
704 general, wind speed is smaller at night, and the four schemes overestimate wind speed much more
705 than during the day. Averaging the RB of wind speed over the five regions and four months, the
706 daytime (nighttime) values for the YSU, ACM2, BL and MYJ schemes are 77.7% (92.4%), 85.6%
707 (123.6%), 80.2% (146.0%), and 100.8% (117.4%), respectively. This simulated misestimation of
708 low winds at night may mainly originate from the inapplicability of the M-O similarity theory. The
709 strong stable boundary layer usually occurs on nights with low winds(Monahan and Abraham, 2019;
710 Vignon et al., 2017). In this strong stable boundary layer, turbulence occurs weakly and
711 intermittently, the turbulence intensity is disproportionate to the mean gradient, and the M-O
712 similarity theory is no longer applicable(Acevedo et al., 2015; Sun et al., 2012). Ultimately, these
713 inapplicable functions affect the calculation of the bulk transfer coefficient and can further lead to
714 large deviations in the simulation of wind speed.
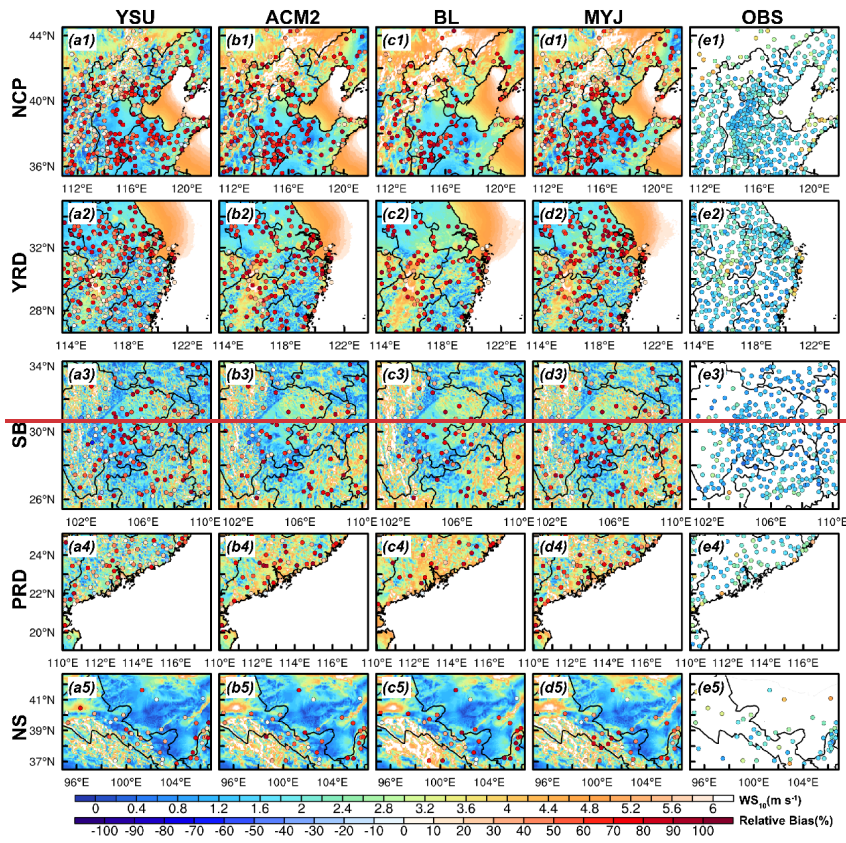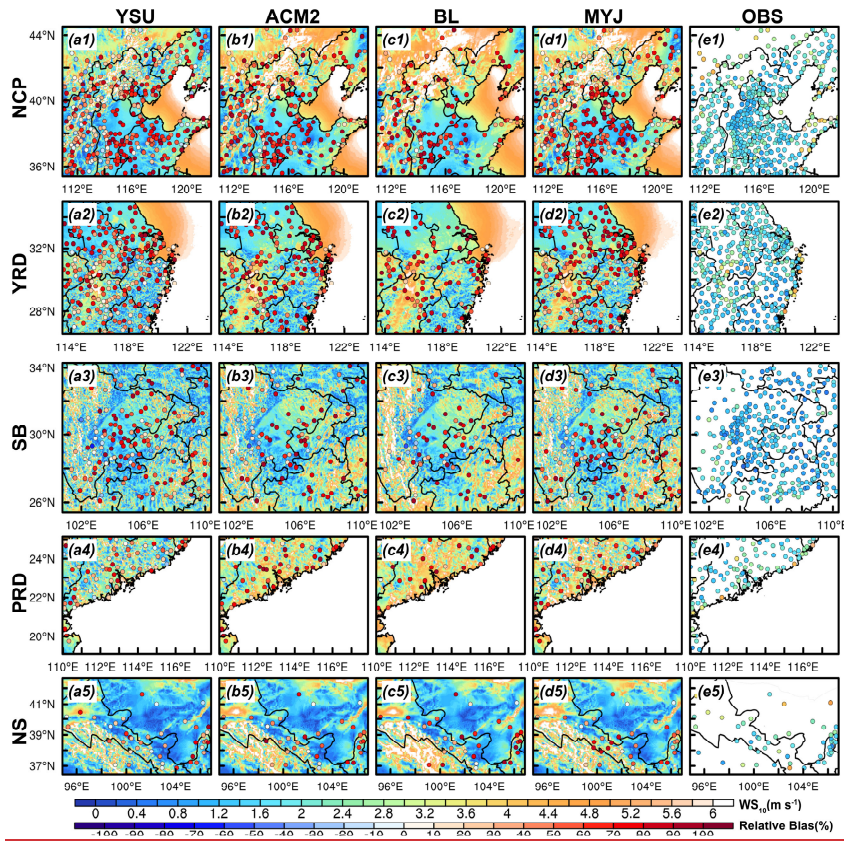
Figure 11. Similar as ~~f~~Figure 6, but for 10-m wind speed.

We further re-analyze the effect of topography on wind speed. The wind speed is overestimated for plains and valleys and better reproduced/underestimated for mountain tops, mainly because of the smoother topography in the model. This is rather because coastal stations in the plains, many of which also have high wind speeds, are not well reproduced and still show significant overestimation (Fig. 10), than the high wind speeds at the top of the mountains, which are better simulated. It is assumed that the wind speed should be small in plain areas with complex underlying surface, but it increases after the model has smoothed the terrain. The wind speed increases gradually with height, and when the terrain at the top of the mountain is smoothed, the originally larger wind speed decreases, and the wind speed will be closer to the observed value.
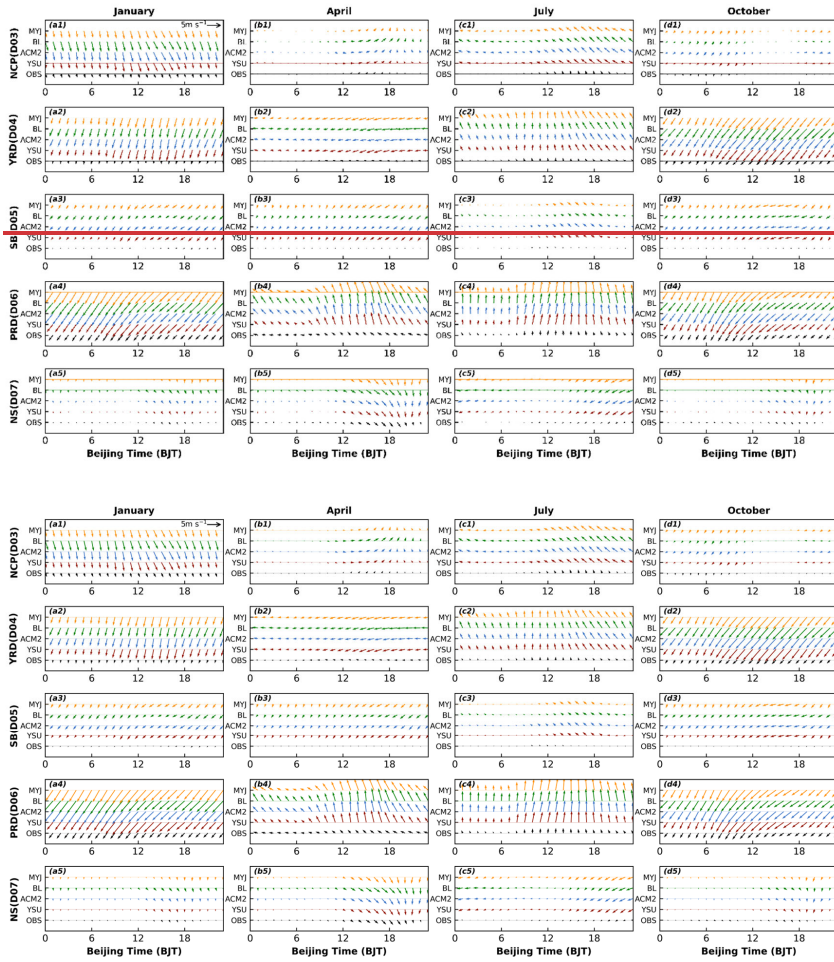
Figure 12. Similar as fFigure 2, but for 10-m wind direction.

The model can basically simulate the changes of wind direction in the five regions, well capturing the overall wind direction in each region (Fig. 12). In the NCP region, the simulation of wind direction is poor in January compared to the other three months, with a high frequency of northwesterly-northerly winds, overestimated by about 6.6% (Fig. 13 a1-d1). In addition, coupled with larger wind speed, it causes the effect of advective transport to be amplified, thus affecting the variation of pollutant concentrations(W. Jia and Zhang, 2021). The frequency of simulated northeasterly winds in the YRD region is higher than that observed in January (~6.9%), April (~6.9%) and October (~11.2%), while the frequency of southerly winds is higher in July (~10.0%) (Fig. 13 a2-d2). The wind direction of SB region is poorly simulated since the topography is too

739 complicated in the SB region, with a basin in the middle and high topographic mountains all around
740 (Fig. 13 a3-d3). The low wind state in the middle of the basin is difficult to be captured. The
741 percentage of northeasterly winds simulated by the model in January, April, July and October are
742 22.9%~25.6%, 19.2%~20.6%, 14.9%~16.4%, 22.4%~24.2%, respectively, and the percentage of
743 observations are 15.1%, 12.0%, 10.9%, 16.1%, respectively. Similarly, the percentage of westerly
744 winds simulated by the model in January, April, July and October are 4.7%~5.1%, 4.7%~5.7%,
745 4.8%~5.5%, 3.8%~5.1%, respectively, and the percentages of observations are 9.9%, 12.4%, 12.4%,
746 12.3%, respectively. The model simulates a large proportion of northeasterly winds and a smaller
747 proportion of westerly winds (Fig. 13 a3-d3). In the PRD region, the frequency of northeasterly
748 wind occurrences in January and October is significantly overestimated by about 8.8% and 9.5%,
749 while the frequency of southerly winds is overestimated in April and July by about 14.5% and 17.3%,
750 and the frequency of southeasterly winds is underestimated (Fig. 13 a4-d4). The wind direction is
751 better simulated in the NS region, not significantly influenced by the complex terrain (Fig. 13 a5-
752 d5).
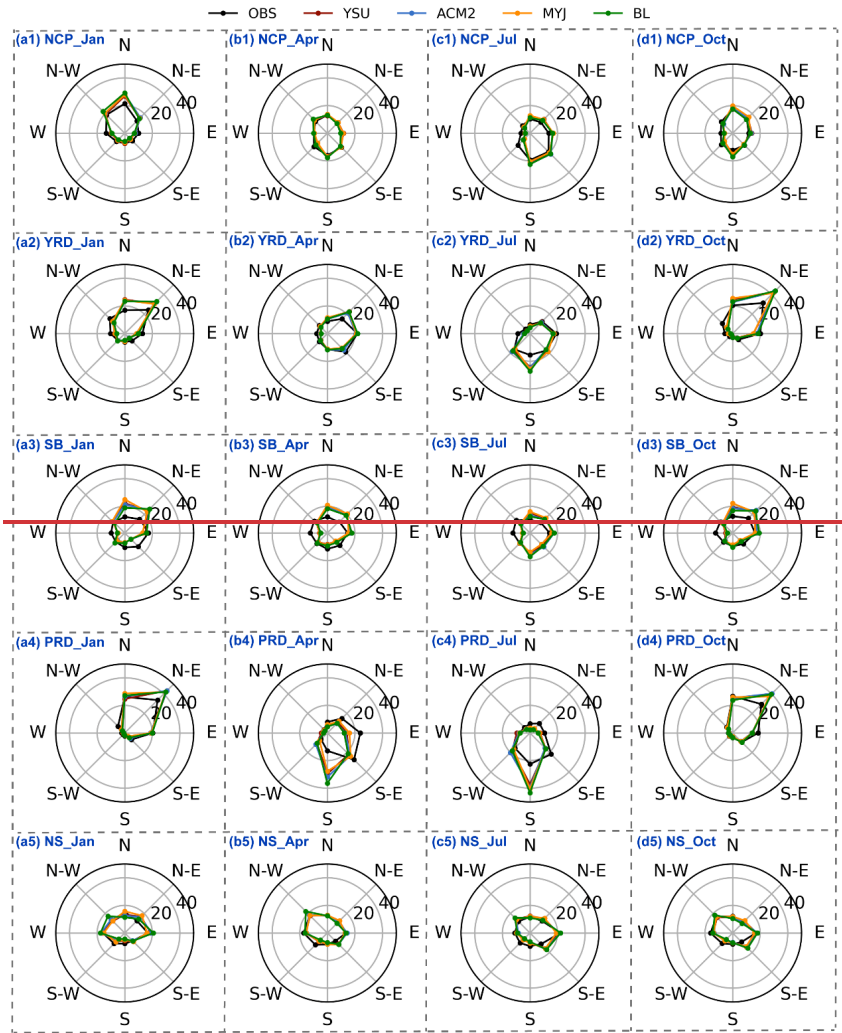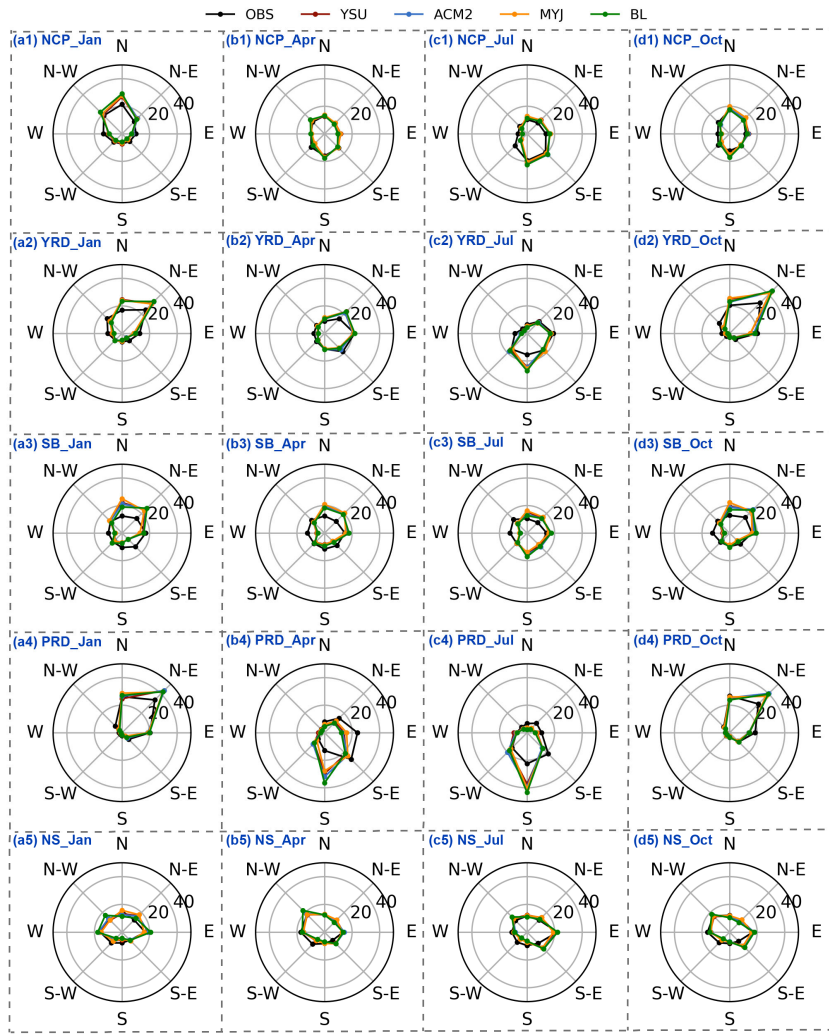
Figure 13. Wind-rose plots in five regions for four seasons are (a1-d1) NCP region, (a2-d2) YRD region, (a3-d3) SB region, (a4-d4) PRD region and (a5-d5) NS region, respectively.

3.2 Vertical structures

To better understand the performance of model in simulating PBL structure under different underlying surface, four representative stations have been selected in each region, with stations in plain areas, stations in mountains areas with high elevation, and stations near the sea.

3.2.1 temperature

Accurate simulation of the vertical structure of the PBL is very important for the evolution of pollution, precipitation and typhoons. In the vertical direction, four typical sounding stations are selected for each region at 08:00 to better reflect the simulation of the vertical structure of the PBL under different underlying surface conditions. Overall, the model captures the vertical structures of the temperature. From the simulation results in January, the best reproduction of the temperature simulation is found in the YRD region, in which the temperature is closer to the observed values (Fig. 14 a2-d2). In addition to the NCP, SB and NS regions, a temperature inversion layer appears in the lower layers at 08:00, and the NS region has the most significant temperature inversion (Fig. 14 a1-d1, a3-d3, a5-d5). The model does not simulate the temperature variation of the inversion layer well, and shows significant differences from the observations. When there is a difference in topography between the observed and simulated stations, the bias in the temperature is more pronounced. These stations usually exist in complex topographic conditions, such as Zhangjiakou and Zhangqiu stations in the NCP region, Shapingba in the SB region, and Mazongshan and Jiuquan in the NS region (Fig. 14 b1, d1, c3, a5, b5). The topographic discrepancy caused by the lack of high resolution may, on the one hand, account for it, resulting in more complex topography in the grid points closest to the observation stations. On the other hand, there is also an urgent need for finer underlying surface data to respond more closely to the observed real topography. The effect of resolution and underlying surface will be discussed in detail in the Part Ⅱ. Although the elevation of the Hongyuan station in the SB region is higher, the difference in topographic height obtained from observations and simulations are close to each other (Fig. 14 a3).

784
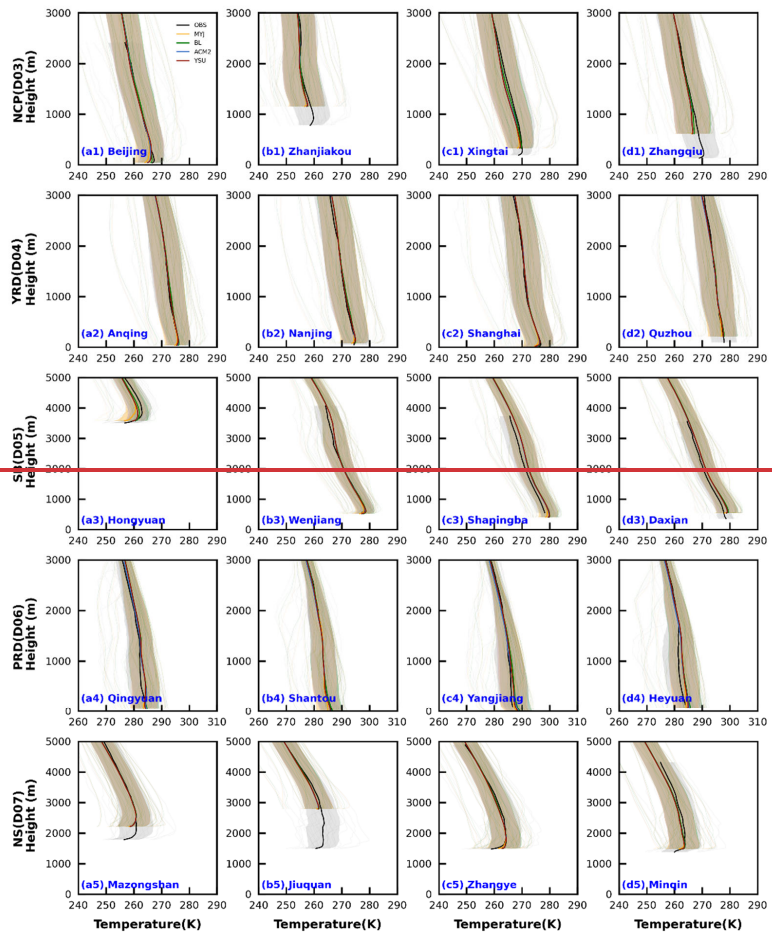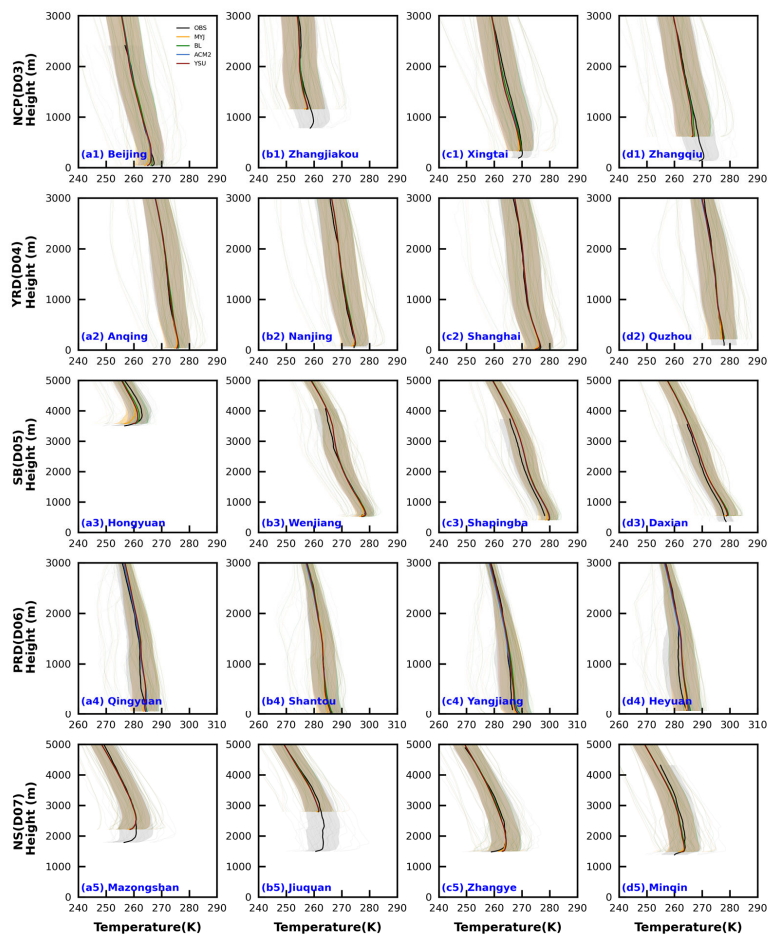
Figure 14. Average vertical profiles of observed and simulated temperature at 08:00 and 20:00 BJT

at four sounding stations for each region in January (Winter). The unobtrusive gray lines indicate

the simulated lines for all time periods, and the lines with shading indicate the average values and

shaded areas show the uncertainty range (the mean ±1 standard deviation).

There is an underestimation of temperature at stations with higher topography and overestimation

for lower topography, which is more consistent with the conclusions drawn from 2-m temperature

(Fig. 5, 14). However, the underestimation of temperature is not present throughout the vertical, but

is more pronounced in the lower layers, which are more influenced by the underlying surface. From

the differences of the four schemes, the MYJ scheme simulates the lowest temperature and largest

temperature gradient. Since the MYJ scheme simulates a weak turbulent diffusion of heat, a well

vertical exchange process cannot occur, bringing into a large temperature gradient (Fig. S19). The

796 differences of the four schemes gradually decrease with the increase of the height. The BL scheme,
797 which is also a local closure scheme, with a smaller vertical gradient in temperature, mainly because
798 this scheme adds a counter-gradient correction term to the heat flux, which is mainly applicable to
799 the convective PBL(Bougeault and Lacarrere, 1989). The presence of this term leads to an increase
800 in turbulent diffusion and a decrease in temperature gradient. However, it is worth noting that there
801 are still slightly stable stratifications at 08:00, and this term generates upward heat flux and reduces
802 the temperature gradient, which is closer to the results of the nonlocal closure schemes (YSU and
803 ACM2 schemes). The simulation results for the other three months are not as good as January, but
804 the simulation characteristics are similar to January (Figures not shown). The results at 20:00 are
805 similar to those at 08:00, and thus will not be repeated here (Figures not shown).

806 **3.2.2 wind speed and direction**

807 The simulation of wind speed vertical structure is much worse in comparison to temperature (Fig.
808 14, 15). The simulated results of wind speed in the vertical direction and 10-m wind speed are still
809 quite different. In the four months, the wind speed is almost overestimated at the lower altitude
810 stations below 1000 m in all the four regions except the NS region, and wind speed is less
811 overestimated in July than in the other three months (Fig. 15, S20-S22 a1-d4). However, for the NS
812 region, the wind speed is almost better simulated, or underestimated, and is significantly different
813 from the other four regions (Fig. 15, S20-S22 a5-d6). We can compare the Zhangjiakou station in
814 the NCP region with the Hongyuan station in the SB region, and find that the wind speeds at these
815 stations are almost not overestimated (Fig. 15 b1, a3). The effect of the model on terrain smoothing
816 contributes to it. Because the wind speed itself increases with the increase of height, and it decreases
817 when the model smooths over the terrain.
818 Unlike the 10-m wind speed, the simulation results of the 10-m wind speed have the smallest bias
819 for the YSU scheme, which is closer to the observed value (Table 2, Figs. 8, 10-11). Of course, this
820 phenomenon can also be found from the evolution of the wind speed in the vertical direction (Fig.
821 15, S20-S22). However, as the height increases, the bias of the YSU scheme gradually increases and
822 is greater than the other three schemes (Fig. 15, S20-S22). Such a large vertical gradient of wind
823 speed in the YSU scheme indicates a weak mixing in this scheme. From the turbulent diffusion
824 coefficients of the momentum at 08:00 in January, it is true that the YSU scheme simulates the
825 smallest turbulent diffusion coefficient below 1000 m (Fig. S23). While the BL scheme simulates a
826 smallest vertical gradient of wind speed, which corresponds to the largest turbulent diffusion
827 coefficient of momentum (Fig. S23). The time variation characteristics of the turbulent diffusion
828 coefficient will be deliberated and analyzed in detail later.
829 The simulation results of wind direction notes that the model can capture the characteristics of wind
830 direction well, and it also simulates well for the stations with more complicated topography and

831 higher altitude (Figs. 15, S20-S22).

833
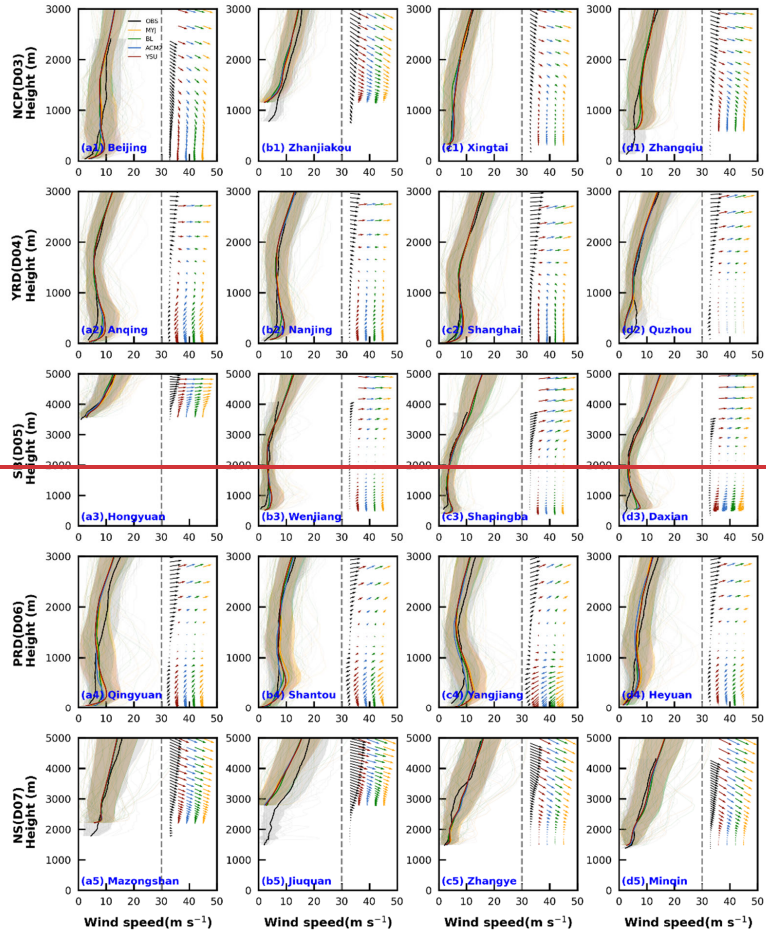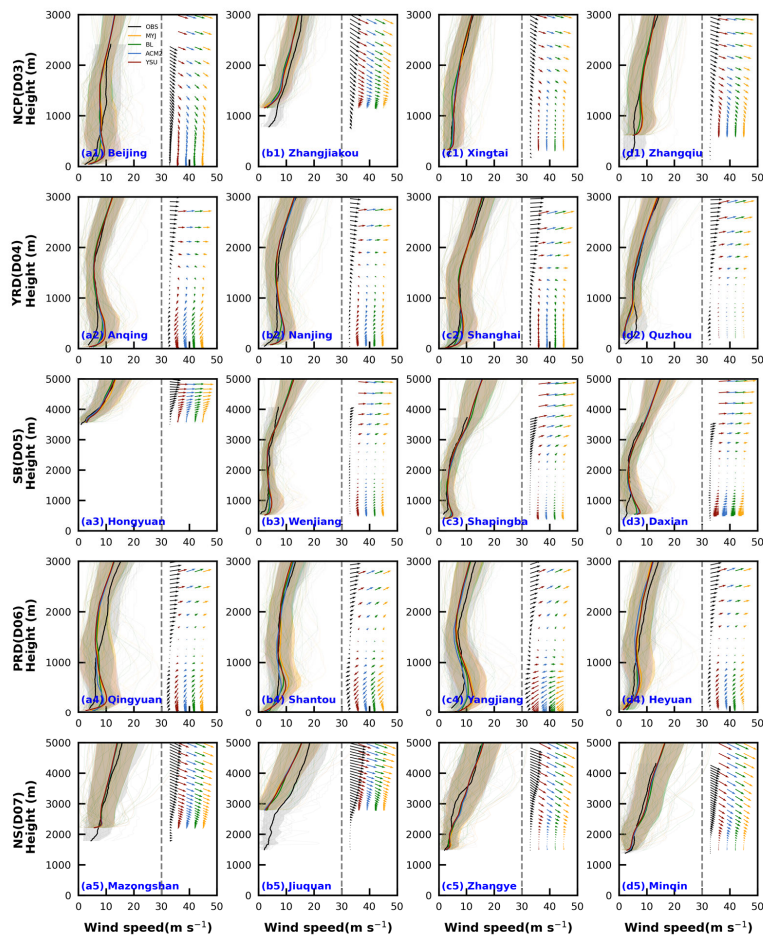
834 Figure 15. Similar as ~~fF~~igure 14, but for ~~10 m~~the vertical profile of wind speed and direction.

835

836 ### 3.3 PBLH

837 Since the observations are only available at 08:00 and 20:00 (Beijing Time, BJT), the comparison

838 of the PBLH are all the results of these two moments. Based on the observed data, comparing the

839 PBLH calculated by the two methods, it is found that the results are mixed for two methods (Fig.

840 16). The results for January (IOA=0.70~0.90) are better than the other three months

841 (IOA=0.44~0.88 in April, IOA=0.51~0.86 in July, IOA=0.60~0.77 in October), and the results in

842 the NCP region are better than the other four regions (Fig. 16). The PBLH in the NS region are more

843 scattered, unlike the other regions where most of the PBLH are concentrated below 500 m,

844 especially in April and July (Fig. 16 b5-c5). On the whole, the difference in PBLH calculated by the
845 two methods is more obvious in the NS region with more complex topography, which is especially
846 noted when calculating in this type of underlying surface region.

847
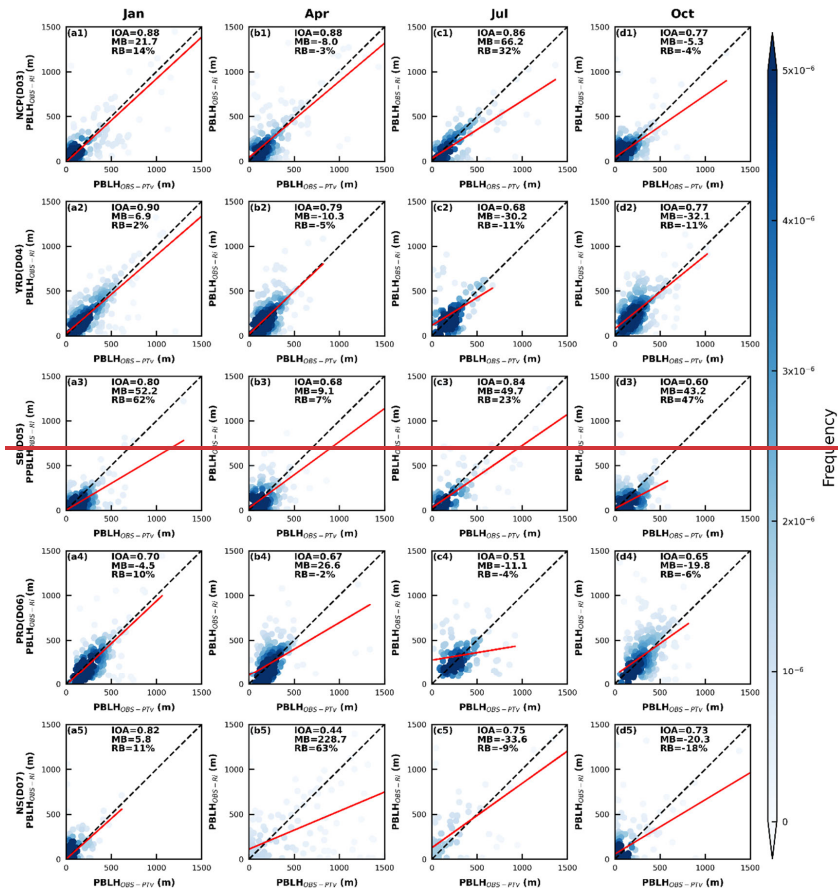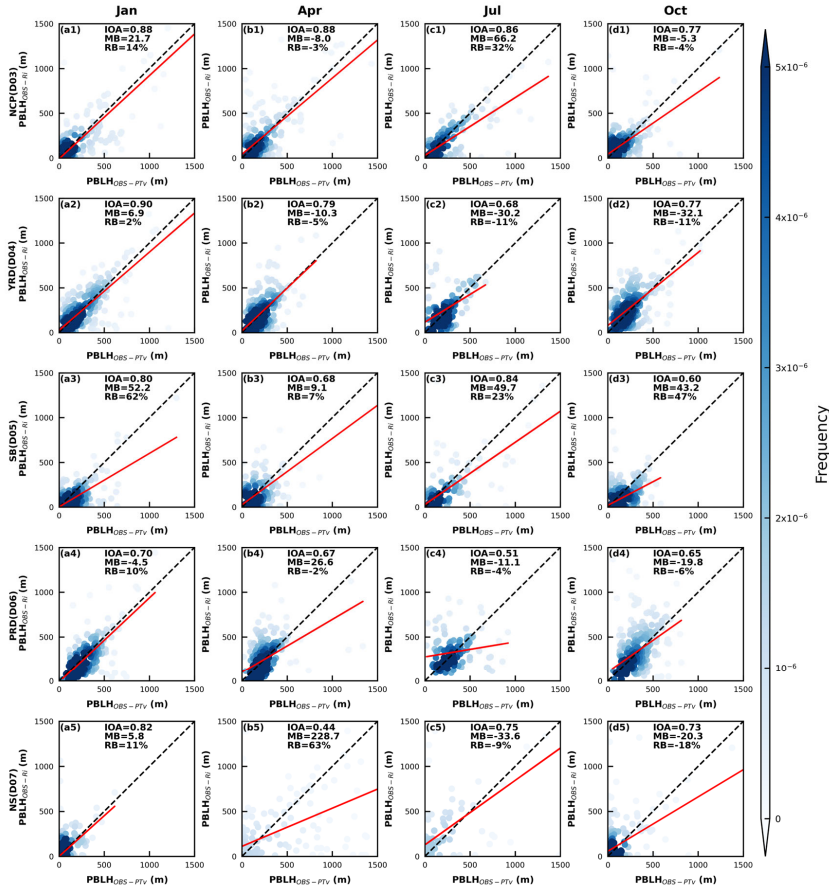
Figure 16. Density scatterplots of the PBLH at 08:00 and 20:00 (Beijing Time, BJT) by the two methods in five regions for four seasons. The horizontal and vertical coordinates represent the PBLH calculated based on the observed data using the virtual temperature method and the Richardson number method, respectively, and IOA, MB, and RB represent the index of agreement, mean bias, and relative bias, respectively.

Further, the mechanism of understanding the PBLH differences based on different stations from different regions. The ~~planetary boundary layer height (~~PBLH~~)~~ for the YSU and ACM2 schemes is calculated by the Richardson number method, and the PBLH for the BL scheme is obtained by the virtual potential temperature method (see Section 2 for details). The same two methods are also used to calculate the PBLH with sounding data for comparison (Eqs. 15~~29~~ and 16~~30~~). First, we compare the PBLH calculated based on the observed data using Richardson number (Ri) with the PBLH simulated by YSU and ACM2 schemes. The Ri is determined by both buoyancy term and the shear

861 term together (Eq. 1529). The difference between simulated and observed temperature gradient is
862 smaller than the wind speed gradient within the PBL (Figs. 14-15). Therefore, the difference in Ri
863 mainly comes from the variation in the shear term. The wind speed gradient simulated in both
864 schemes are greater than the observed values (Fig. 15), except for individual stations, which would
865 result in small values of Ri. Thus, the height of Ri up to 0.25 would be high and the PBLH would
866 be high. Consequently, the PBLH simulated by the YSU and ACM2 schemes are higher than the
867 observed values at most stations. For example, in the case of the Quzhou station in the YRD region,
868 the simulated wind speed gradient at this station is much smaller than the observed value in January,
869 thus, the simulated PBLH is correspondingly smaller than PBLH calculated from observations (Figs.
870 15, S24 d2). Comparing the results of the other three months, we can also find similar conclusions
871 (Figures not shown). The wind speed gradient simulated by the YSU scheme is larger than that of
872 the ACM2 scheme, and therefore the PBLH is larger than that of the ACM2 scheme, except for the
873 Shanghai station in the YRD region, Shantou and Yangjiang stations in the PRD region (Fig. S24).
874 For the ocean, the PBLH simulated by the ACM2 scheme is higher than that of the YSU scheme,
875 while for most areas adjacent to the ocean, the PBLH simulated by the ACM2 scheme is on the high
876 side in the YRD and PRD regions (Fig. S25). The simulated PBLH of the BL scheme is in better
877 agreement with the PBLH calculated by the virtual potential temperature method, which is
878 substantially better than the other three schemes. The PBLH simulated by the MYJ scheme is mixed
879 (Fig. 17).
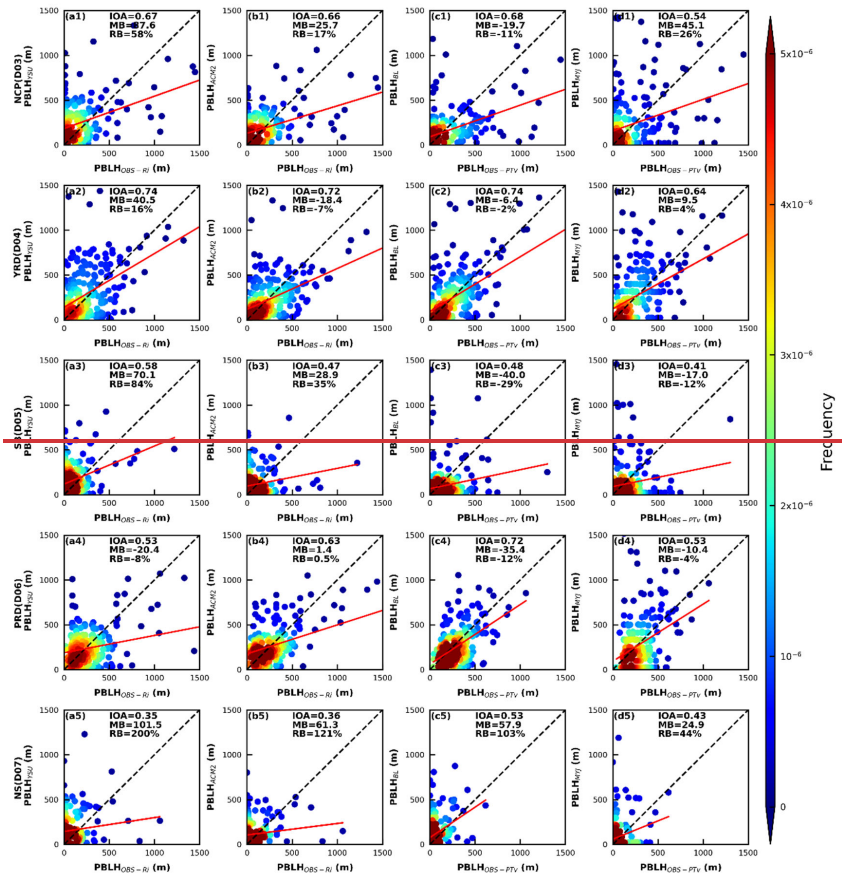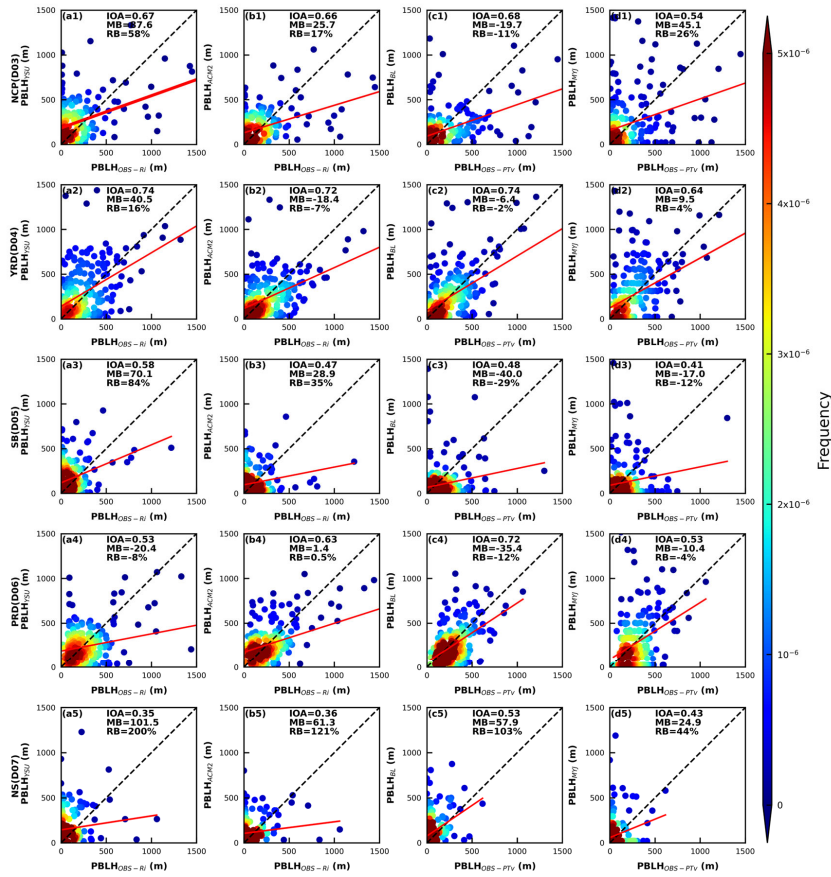
881

882 **Figure 17. Density scatterplots of observed and simulated PBLH** at 08:00 and 20:00 (BJT) **by four**

883 **PBL schemes in five regions in January (Winter).** The horizontal and vertical subscripts YSU,

884 ACM2, BL, and MYJ indicate the four schemes, and OBS-Ri and OBS-PTv indicate the

885 Richardson number method and virtual popential temperature method, respectively.

886 From the differences of regional distributions, the region with the best PBLH simulation results is

887 the YRD region in January, (IOA=0.64~0.74; MB=-6.4~40.5 m; RB=-2%~16%), followed by the

888 PRD region (IOA=0.53~0.72; MB=-35.4~1.4 m; RB=-12%~0.5%), and the worst simulation results

889 for the PBLH in the NS region (IOA=0.35~0.53; MB=24.9~101.5 m; RB=44%~200%) (Fig. 17).

890 Also, the PBLH simulation in the SB region is poorer and slightly better than that in the NS region,

891 noting that there is still much potential for the model to improve the reproduction of the PBLH in

892 complex terrain. From the simulation results of the four schemes, the PBLH simulated by the BL

893 scheme is the closest to the observed value, followed by the YSU and ACM2 schemes, and the

PBLH simulated by the MYJ scheme is the worst. However, it is worth noting here that the method for calculating the PBLH in the MYJ scheme is the TKE, and there is still some uncertainty in the comparison using the virtual potential temperature method. The simulation results of temperature are better than other meteorological parameters, therefore, the PBLH calculated in the model using the virtual potential temperature method is more consistent with the observed results.~~in that the simulation results of temperature are better compared with other meteorological factors, so the method of judging the PBLH using the virtual potential temperature will be more consistent with the observed values.~~ While as the YSU and ACM2 schemes using Richardson number method will involve the wind speed gradient, and the vertical gradient of wind speed is poorly simulated below 1000 m. That's why it will affect the judgment of the PBLH. If the simulation results of vertical gradient of wind speed can be improved subsequently, then the simulation results of PBLH of these two schemes will be improved to some extent. There are not enough observations to calculate the PBLH using TKE, so there will be some differences with the PBLH simulated by the MYJ scheme. The mean bias of the simulation increased in April and July when the PBLH is higher compared to January, with mean bias of -29.6~361.8 m (6.5~603.9 m), -12.6~410.6 m (41.6~603.2 m), -34.1~301.1 m (3.2~683.9 m) and -14.5~96.3 m (-11.3~523.6 m) for the YSU, ACM2, BL and MYJ schemes in April (July), respectively. Similar to January, the best simulation results have been obtained for the YRD (MB=7.8~72.4 m in April, MB=28.5~66.5 m in July) and PRD (MB=-34.1~-12.6 m in April, MB=-11.3~54.8 m in July) regions, and the worst for the NS region (MB=61.8~410.6 m in April, MB=523.6~683.9 m in July). The results for October are more similar to those for January, with lower PBLH and better simulations than those for April and July (Figures not shown).

3.4 turbulent diffusion coefficient

Since the model itself does not directly output turbulent diffusion coefficients for all schemes, there is relatively little direct comparison and analysis of this parameter. As seen in section 3.2~~3~~.2 above, the ~~turbulent diffusion coefficient~~ (TDC) plays a crucial role in the momentum vertical transport within the PBL and also has an impact on the diffusion of other parameters, such as heat, water vapor and pollutants (Ding et al., 2021; R. B. Stull, 1988). The accurate portrayal of the TDC directly affects the evolution of the PBL structures. Based on the contents of section 2.3, the momentum TDC is not equal to the heat TDC under unstable and neutral conditions for the YSU scheme, and the momentum TDC is equal to the heat TDC under stable conditions. The ACM2 scheme uses the MOST method to calculate the TDC as the YSU scheme, but also considers the TDC calculated by the mixing length theory. The momentum TDC is not equal to the heat TDC in the MYJ scheme, while the momentum TDC is equal to the heat TDC in the BL scheme. Because of the difference in altitude of different stations, Bejing station in the NCP region, Nanjing station in the YRD region,

929 Daxian station in the SB region, Qingyuan station in the PRD region and Zhangye station in the NS

930 region were selected as representative stations to analyze the turbulent diffusion characteristics.

931 Here, the TDC of heat is taken as an example, the following basic characteristics have been found.

932 (1) the YSU and MYJ schemes have the largest TDC during the day, followed by the BL scheme,

933 and the ACM2 scheme has the smallest TDC (Fig. 18). (2) The TDC is largest in April and July, and

934 smallest in January and October (Fig. 18). (3) There are significant seasonal differences in the PBLH

935 for the NCP, SB and NS regions, while for the YRD and PRD regions (Figures not shown). The

936 difference in the PBLH affects the variation of the turbulent diffusion, especially for the YSU and

937 ACM2 schemes, where the PBLH is used during the calculation of the turbulent diffusion. In the

938 YSU scheme, the TDC of momentum is calculated first, and then the TDC of heat is calculated with

939 the Prandtl number (Pr). Thus, the variation of the PBLH is proportional to the TDC (Fig. 18a).

940 While in the ACM2 scheme, the TDC of heat is calculated directly based on the dimensionless

941 function of heat. Moreover, the Pr in the YSU scheme varies with height, while the Pr in the ACM2

942 scheme is a constant (=0.8). It is also worth noting that in the ACM2 scheme, another TDC is

943 calculated using the mixing length theory, and the change of the empirical stability function in the

944 mixing length method changes the TDC. Therefore, the YSU scheme calculates a large TDC of

945 momentum, which also leads to a large TDC of heat. The TDC of heat in the ACM2 scheme, on the

946 other hand, will be affected by the mixing length method, and differs from the calculation principle

947 of the YSU scheme.
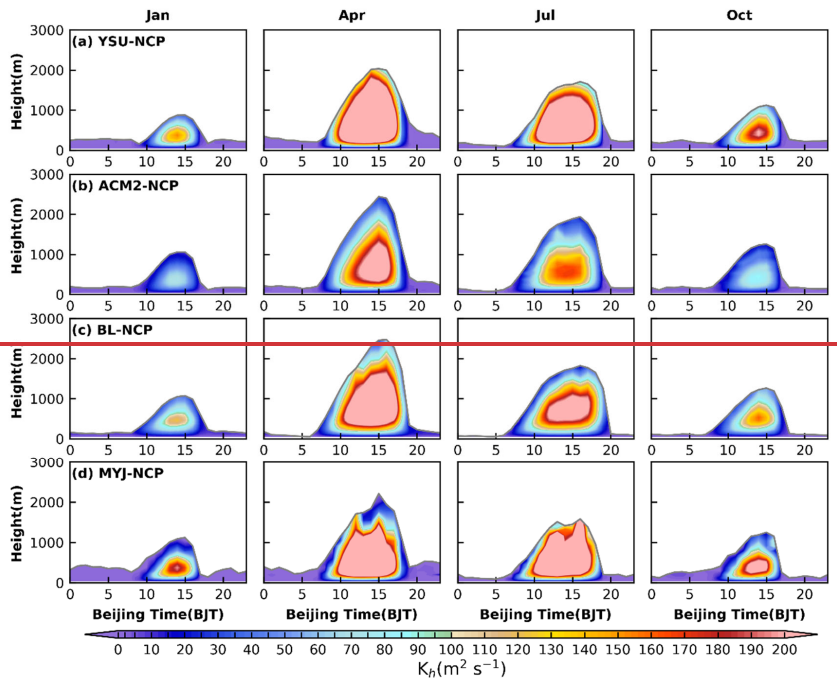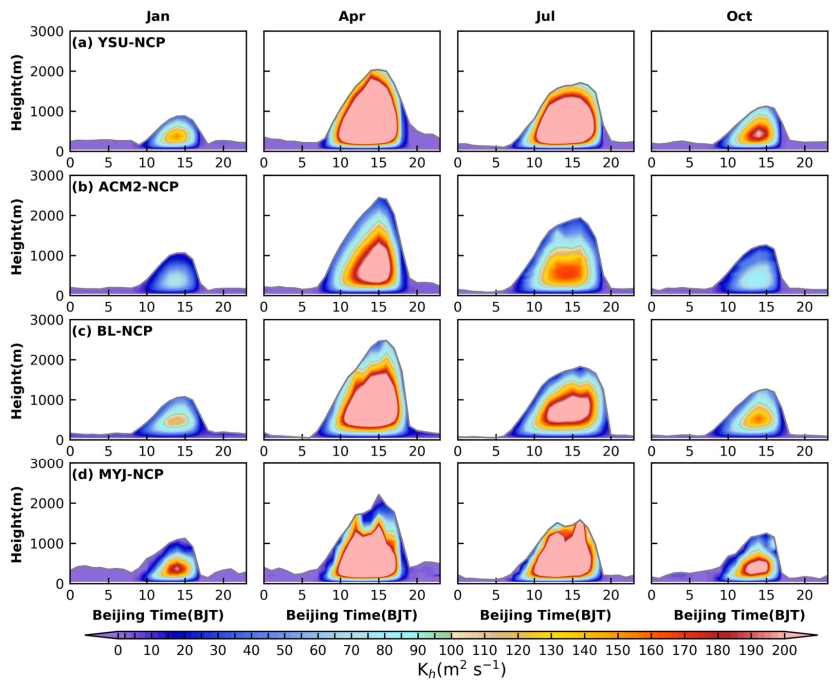
Figure 18. Time-height cross sections of heat turbulent diffusion coefficient simulated by (a) YSU scheme, (b) ACM2 scheme, (c) BL scheme and (d) MYJ scheme for four seasons in the NCP region. The gray line indicates the PBLH.

From the section 3.2.2 above, it is clear that the BL scheme has the strongest turbulent diffusion at 08:00, making the vertical gradient smaller, especially the wind speed is large. Similarly, this phenomenon can be found in the daily variation of turbulent diffusion, and not only at 08:00, but almost throughout the night (Fig. 18). The difference between MYJ and BL schemes is mainly reflected in the calculation principle of mixing length, which is not directly related to the PBLH. In the BL scheme, mixing length scale can be relative to the distance that a parcel originating from this layer, can travel upward and downward before being stopped by buoyancy effects (Eq. 14). Therefore, the vertical height below the temperature inversion layer at night, with the surface as the lower boundary, is the length scale of turbulence, i.e., mixing length scale. While in the MYJ scheme, the mixing length scale is equal to z minus the integral depth scale, which is equal to the height of the equal-area rectangle under the profile. It is worth noting that the mixing length scale in the BL scheme mainly considers the effect of thermal and takes temperature gradient as the criterion, while the turbulent length scale in the MYJ scheme is mainly determined based on the TKE. TKE is further divided into horizontal TKE and vertical TKE. Horizontal TKE is mainly influenced by wind shear and the turbulent eddy scale can reach 1.5~3 times the PBLH on the horizontal, and even reach 6 times the PBLH(Atkinson and Zhang, 1996). The vertical depth of an unstable layer capped by an inversion is automatically selected as the length scale for turbulence in the BL scheme during the daytime. Moreover, in the BL scheme, there is a counter-gradient correction term in the convective PBL, which leads to a downward transport of dry and cool air, making the thermal reach a lower height and a smaller length scale for turbulence(Bougeault and Lacarrere, 1989). We also find that the PBLH of the MYJ scheme exhibits a "sawtooth", and is more pronounced at night. This is mainly because the turbulence is weaker at night, and presents intermittent characteristics, which, together with the judgment method of PBLH and the coarse vertical resolution, can cause such variation of the PBLH. Although the improvement of PBLH in the MYJ scheme cannot have a substantial effect on turbulent diffusion, the threshold value of its determination method is open to question.

3.5 Discussion of optimal PBL schemes

To better understand the simulation performance of different PBL parameterization schemes for different parameters in each region, this section will discuss the expressiveness of different PBL schemes through the statistical approach. Figure 19 shows the Taylor statistics for the analysis of near-surface meteorological parameters in four months in five regions.
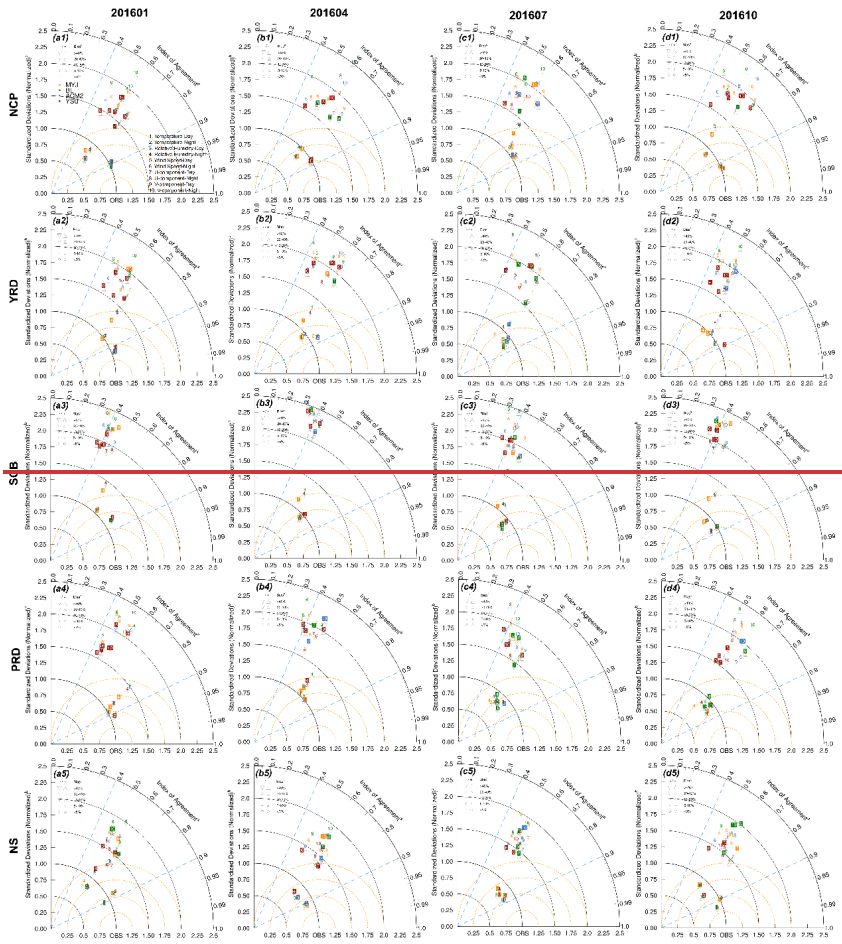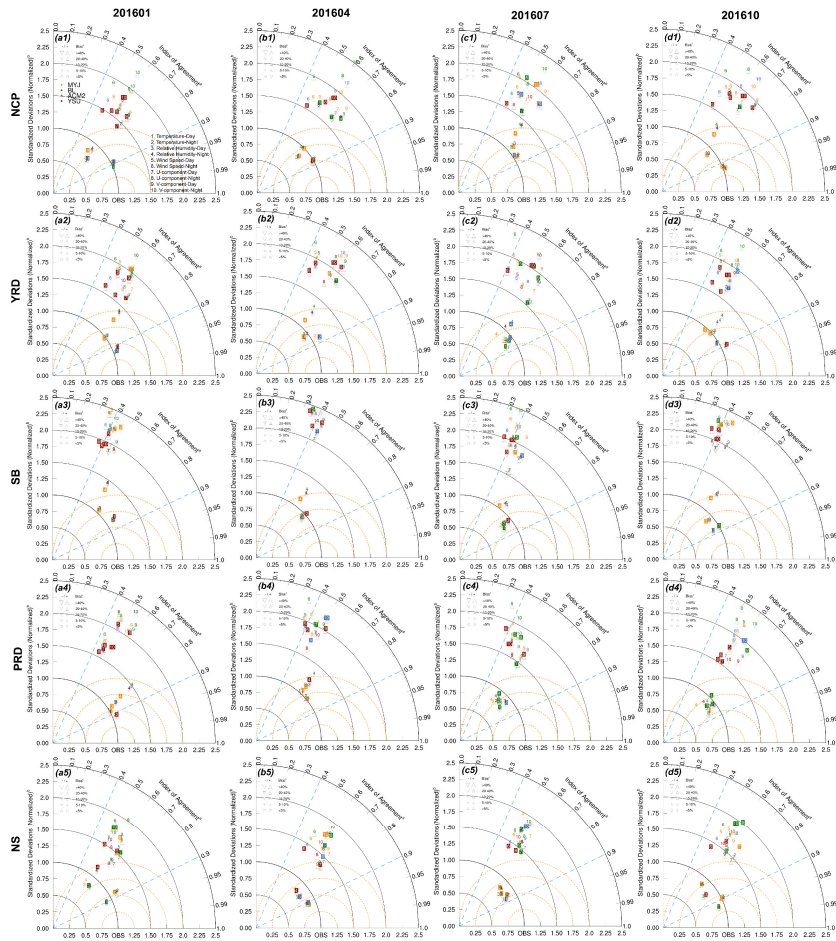
Figure 19. Taylor diagram of observation and simulation in five regions for four seasons. XY axes and arc represent the normalized standardized deviations (NSDs; NSD = $\frac{\sqrt{\frac{1}{N-1}\sum_{i=1}^{n}(X_{sim,i}-\overline{X_{sim}})^2}}{\sqrt{\frac{1}{N-1}\sum_{i=1}^{n}(X_{obs,i}-\overline{X_{obs}})^2}}$, $\overline{X_{sim}}$ and $\overline{X_{obs}}$ represent the average value of simulation and observation, respectively) and index of agreement (IOA; IOA = $1 - \frac{[\sum_{i=1}^{n}|X_{sim,i}-X_{obs,i}|^2]}{[\sum_{i=1}^{n}(|X_{sim,i}-\overline{X_{obs}}|+|X_{obs,i}-\overline{X_{obs}}|)^2]}$, $X_{sim,i}$ and $X_{obs,i}$ represent the value of simulated and observed, respectively; *i* refers to time, and *n* is the total number of time series), respectively. Four schemes are shown in different colors, and different numbers represent different parameters. The root mean square is denoted by orange dashed line and the relative bias (RB; RB = $\frac{\overline{X_{sim}}-\overline{X_{obs}}}{\overline{X_{obs}}} \times 100\%$) is shown by different symbols.

For the NCP region, the 2-m temperatures are underestimated during the daytime in January (Fig. 2), while the BL scheme simulates the highest temperature, so the BL scheme performs optimally. Although the temperatures are somewhat overestimated at night, the overestimated period is shorter. The IOA of the four schemes is similar, with the ACM2 scheme having a slightly smaller bias (Fig. 19 a1). Combined with the regional distribution of all stations in the NCP region, the BL scheme is recommended if the study area is mainly for Beijing, while the ACM2 and YSU schemes are recommended for the south of the NCP in January, such as Shandong Peninsula and southern Hebei province. For the other three months, temperatures are overestimated to varying degrees, both during the day and at night (Fig. 2). The MYJ scheme performs best in all statistical parameters at night (Fig. 19 b1-d1), while during the daytime, it slightly underperforms the YSU and ACM2 schemes in relative bias in January and April, but the difference is not very distinct. Therefore, for the simulation of 2-m temperature in other three months, the MYJ scheme would be more recommended. In the YRD region, the 2-m temperatures are overestimated during the daytime, the BL schemes show overestimation at night, the MYJ scheme show underestimation, and the YSU and ACM2 schemes perform optimally (Fig. 2 a2-d2). According to the Taylor statistical parameters, it can be seen that the ACM2 scheme performs better than the YSU scheme in the four months, and based on that, the ACM2 scheme is recommended (Fig. 19 a2-d2). The 2-m temperature in the SB region during the daytime is the same as in the YRD region, and the ACM2 scheme performs optimally (Fig. 19 a3-d3). However, the BL scheme performs optimally during the nighttime, except in April (Fig. 19 b3). The PRD region differs from the other regions in that the temperature simulation is significantly higher in January and April, and the MYJ scheme performs best in both daytime and nighttime (Fig. 19 a4-b4). In contrast, the temperature simulation bias less in July and October, and the BL scheme performs best (Fig. 19 c4-d4). The 2-m temperature are almost underestimated during the daytime and overestimated for the nighttime in the NS region, and the MYJ scheme outperforms other schemes on account of its large diurnal temperature range (Fig. 19 a5-d5). Of course, the BL scheme presents a slight advantage in the relative bias during the daytime in January (Fig. 19 a5).

The results of 2-m relative humidity are relatively uniform, and the MYJ scheme shows optimal simulation performance in almost all months in all regions. Except for July in the YRD region, July and October in the PRD region, and January and April in the NS region (Fig. 19 c2, c4-d4, a5-b5). For the simulation of 10-m wind speed and direction, the YSU scheme shows a very clear advantage, which is outstanding in all regions and all months (Fig. 19).

Several sounding stations with large differences between the observed and simulated altitudes are removed. Then, the stations in each region are averaged to induce the variation characteristics from 100 m to 2000 m in vertical.

1028
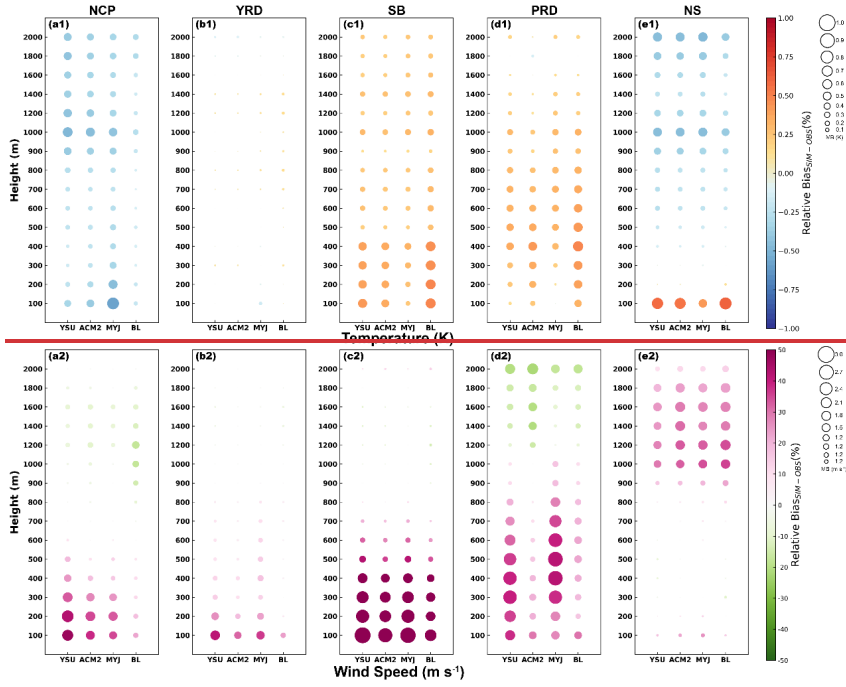
1029
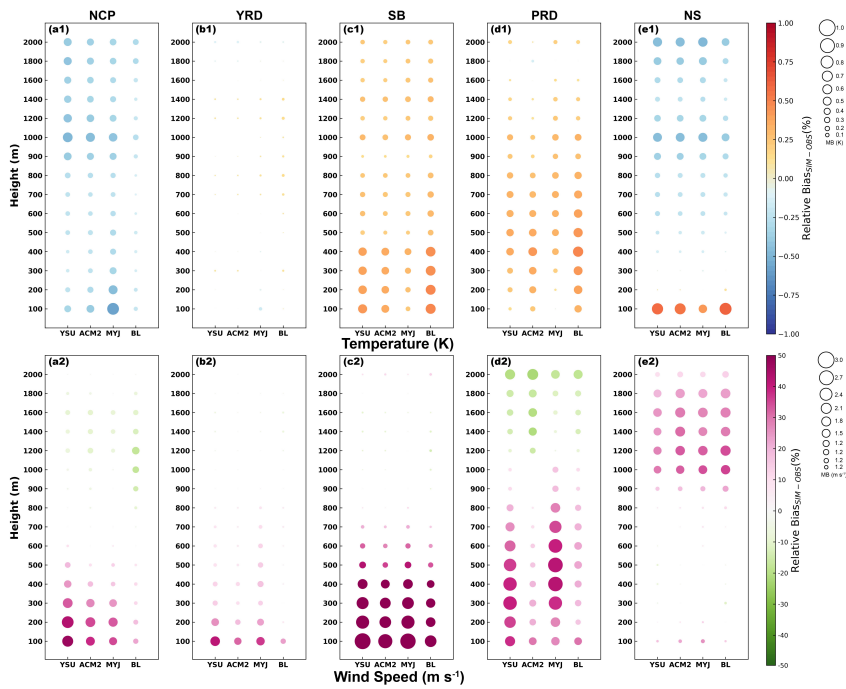
Figure 20. Statistics of temperature and wind speed in different layers at vertical height in January (Winter), with circle size indicating the mean bias between simulations and observations, and circles filled with color denoting the relative bias.

The BL scheme has the smallest simulation bias for the temperature in the vertical direction in January for the NCP region, and performs optimally, which is associated with the discussion of the optimal scheme for the 2-m temperature (Fig. 20 a1) to some degree. While in all the other three months, the MYJ scheme has the smallest bias and is consistent with the conclusion of the 2-m temperature (Fig. S26-S28 a1). In the YRD region, there is no clear difference between the four schemes for the simulation of temperature in the vertical direction, and the deviation of the simulation in January is less than 0.1 K (Fig. 20 b1). The optimal scheme for 2-m temperature can be considered as a representative choice. The MYJ scheme has a better simulation of the vertical profile of the temperature that is somewhat different from the most preferred scheme of 2-m temperature in the SB region (Fig. 20, S26-S28 c1). This is mainly because the selected sounding stations are basically located in the basin area with low elevation, and the temperatures are overestimated, as is the 2-m temperature (Fig. 5). If the stations around the basin are not considered, the simulation of 2-m temperature will also be overestimated and the MYJ scheme also perform optimally. There is no complex topography in the PRD region, the results from the sounding stations and surface layer can be well echoed. In the vertical direction, the MYJ simulates the vertical profile of temperature better, particularly in January and April (Fig. 20, S30, d1). While in July and October, the simulation results of the four schemes have little difference, especially in the lower level, which can be represented by the optimal scheme of 2-m temperature (Fig. S27-S28, d1). For the NS region, there is an overestimation in the lower levels and an underestimation in the upper levels for each month. The height of overestimation is lower in January and April, around 200 m, while it can reach around 500 m in July and October (Fig. 20, S26-S28, e1). The positive deviation decreases as the height increases, but after reaching a certain height, the negative deviation increases again. In the process of decreasing the positive deviation with height, the MYJ scheme performs the best, which is consistent with the 2-m temperature. While the BL scheme performs slightly better when the negative deviation gradually increases with height.

For wind speed, the YSU scheme is optimal for 10-m wind speed for all regions and months. However, the quite different in terms of the variation of vertical wind speed. Throughout all regions and months, the simulation bias of the BL scheme is the smallest and closer to the observation, which is also the results obtained from the section 3.2.2 (Fig. 20, S26-S28 a2-e2). The stronger turbulent diffusion of the BL scheme at 08:00 makes the wind speed more uniformly mixed in the vertical direction. And the vertical variation characteristics at 08:00 can be extended to the whole night. But during the daytime, the result may not be the same, after all, the vertical mixing of the YSU scheme is stronger, and does not produce such a large wind speed gradient.

1066 In general, in the selection process of the PBL scheme, if the focus is on temperature variation, such
1067 as temperature inversion, the optimal scheme for both 2-m temperature and vertical temperature can
1068 be considered, and there is basically no significant difference. However, if the focus is on the
1069 variation of wind speed, wind energy, then the vertical wind speed and in the surface layer need to
1070 be evaluated and selected with comprehensive consideration.

1071 **4 Conclusion**

1072 The ~~planetary boundary layer~~PBL serves as a bridge between the ground and the free atmosphere,
1073 and its role cannot be ignored. Turbulence, as the primary motion within the PBL, controls the
1074 vertical mixing of heat, water vapor, momentum, and pollutants. Turbulence as a sub-grid-scale
1075 motion is usually parameterized in the model, i.e., PBL parameterization scheme. The most widely
1076 used mesoscale model (i.e., WRF), which has developed 12 schemes, includes nonlocal closure
1077 scheme, local closure scheme and hybrid nonlocal-local closure scheme. Across the world, there
1078 have been many evaluation studies for PBL parameterization schemes (reference Fig. 1 in Jia and
1079 Zhang, 2020). However, most of the studies have been conducted for individual stations in a small
1080 region with special individual cases for research and analysis, which are not well represented and
1081 applied. Meanwhile, there is a deficiency in understanding the mechanism of the scheme itself. In
1082 response, aiming at the current research deficiencies, four typical schemes (YSU, ACM2, BL and
1083 MYJ, covering each type scheme) are selected in this study to evaluate and analyze the near-surface
1084 meteorological parameters, vertical structure of the PBL, PBLH and turbulence diffusion in four
1085 months (i.e., January, April, July and October) in five typical regions of China (i.e., NCP, YRD, SB,
1086 PRD and NS regions).

1087 *a. 2-m temperature.* (1) In terms of time series and diurnal, the simulation results for July are better
1088 than the other three months, and better at night than daytime, with less deviation between simulation
1089 and observation. (2) in terms of regional distribution, temperatures at stations with higher elevations
1090 are easily underestimated (e.g., mountainous areas in the NCP region, areas around the SB basin,
1091 and the NS region), while overestimated at plains and basin (e.g., YRD, PRD and the SB basin
1092 regions), and the overestimation/underestimation is more significant during the daytime. (3) In
1093 terms of mechanism differences between schemes, the differences in the simulated temperatures of
1094 the four schemes are more pronounced at night. The differences in simulated temperatures between
1095 the nonlocal scheme mainly originate from downward shortwave radiation, while the effects of
1096 sensible heat flux (HFX) need to be further ruminated when comparing with the local closure
1097 scheme. when analyzing the HFX, the gradient of 2-m temperature and surface temperature, the
1098 variation of heat transfer coefficient need to be discussed in detail.

1099 *b. 2-m relative humidity.* The changes in relative humidity and temperature correspond to each other,
1100 and again the best simulation results are obtained in July. Except for the NS region, the relative

1101 humidity of the other regions is underestimated.

1102 *c. 10-m wind speed.* (1) The simulation bias is the largest for the MYJ scheme during the daytime

1103 (except for the NCP region), and the BL scheme presents the largest deviation at night in all regions,

1104 and the difference is not significant in the four months. The variation of 10-m wind speed is

1105 influenced by the momentum transfer coefficient, where a larger C_m produces stronger mixing and

1106 transports more momentum from the upper layers to the lower layers. For the YSU, ACM2 and BL

1107 schemes, the C_m and 10-m wind speed vary proportionally. In contrast, the MYJ scheme calculate

1108 principle of for MYJ scheme is different from the other schemes, and the C_m is larger than other

1109 months almost all day. However, the wind speed simulated by the MYJ scheme is maximum only

1110 during the daytime, which indicates that it is influenced by integrated similarity functions. (2) In

1111 terms of regional distribution, the wind speed is more overestimated in plains and basins, and less

1112 overestimated or even underestimated in mountainous areas. This is chiefly due to the influence of

1113 the model on terrain smoothing. (3) The overestimation of smaller wind speed at night is more

1114 obvious in the four schemes, primarily owing to the non-application of the MOST. At night, the

1115 turbulence intensity is disproportionate to the mean gradient, and the M-O similarity theory is no

1116 longer applicable.

1117 *d. 10-m wind direction.* The simulation of wind direction in January for the NCP region worse than

1118 the other three months, and the frequency of simulated northwest-north winds is overestimated by

1119 about 6.6%. For the YRD region, the frequency of northeasterly winds is overestimated. The

1120 simulation of wind direction in the SB region is not as good as other regions due to the complex

1121 topography. The frequency of northeasterly winds is overestimated in January and October in the

1122 PRD region, and that of southerly winds is overestimated in April and July. The wind direction is

1123 better simulated for the NS region, and the difference is not very obvious.

1124 *e. ~~vertical distribution of~~ PBL vertical structures.* The model can reproduce the vertical structure

1125 of temperature well, but the inversion temperature at the lower levels of many stations in complex

1126 terrain cannot be simulated well, mainly because there is a certain difference in the terrain height

1127 between observation and simulation. At 08:00, the MYJ scheme simulates the lowest temperature

1128 and the BL scheme for the highest temperature, and the difference is more conspicuous at the lower

1129 levels. The vertical structure of the wind speed is clearly not as good as the temperature. The wind

1130 speed is almost always overestimated below 1000 m, except for the NS region. Unlike the 10-m

1131 wind speed, YSU has the smallest deviation from the 10-m wind speed, while the BL scheme has

1132 the smallest bias in the vertical direction. The BL scheme has the largest turbulent diffusion and the

1133 strongest mixing at 08:00.

1134 *f. PBLH.* The PBLH calculated based on the observed data using the two methods are better in

1135 January than in the other three months, and in the NCP region than in the other four regions. The

1136 wind speed gradient simulated by the YSU scheme is large, resulting in a small Richardson number

1137 (Ri), making the height higher when Ri reaches 0.25, and the PBLH is higher than that of the ACM2
1138 scheme. The PBLH simulated by the BL scheme is closer to the observation because the temperature
1139 gradient is best simulated. The MYJ scheme results in a jagged variation of the PBLH due to the
1140 determination of the threshold and the vertical resolution, and this phenomenon is especially
1141 obvious at night. In terms of regional distribution, the PBLH is best simulated in the YRD region,
1142 followed by the PRD region and worst in the NS region. The results are similar in January and
1143 October, when the PBLH is lower and the simulations are better than those in April and July.
1144 *g. turbulent diffusion coefficient.* (1) The TDC simulated by the YSU and MYJ schemes is the
1145 largest during the daytime, followed by the BL scheme, and the smallest by the ACM2 scheme. The
1146 TDC simulated by the BL scheme is the largest at night, and the other three schemes are about the
1147 same. (2) The TDC is maximum in April and July, and minimum in January and October. (3) The
1148 obvious difference in PBLH affects the turbulent diffusion of the YSU and ACM2 schemes. It is
1149 worth noting that the YSU scheme calculates the TDC of momentum first, and then uses Prandtl
1150 number (Pr) to calculate the TDC of heat, while the ACM2 scheme calculates the TDC of both
1151 momentum and heat. (4) The difference between the BL and MYJ schemes is mainly reflected in
1152 the calculation principle of mixing length. The buoyancy effect mainly affects the mixing length
1153 scale in the BL scheme, and the mixing length scale of MYJ scheme is influenced by the TKE.
1154 For the discussion of the optimal scheme, different schemes need to be proposed for different
1155 parameters. (1) Temperature. The BL scheme is recommended for January in the NCP region,
1156 especially for the Beijing, and the MYJ scheme is recommended for the other three months. The
1157 simulation difference between the four schemes is small in the YRD region, and the ACM2 scheme
1158 is recommended. The topography is more complex in the SB region, but the MYJ scheme is
1159 recommended for most areas within the basin, and the BL scheme is recommended for the SB region
1160 if more around basin is involved. The MYJ scheme is recommended for the PRD region in January
1161 and April, and the BL scheme is recommended for July and October. In the NS region, the MYJ
1162 scheme is recommended. (2) Relative humidity. The MYJ scheme is recommended for all regions
1163 in four months. (3) Wind speed. The YSU scheme is recommended if the main concern is the surface
1164 layer, and the BL scheme is recommended if the focus on the variation of wind speed in the vertical
1165 direction.
1166 The PBL parameterization scheme, as the most critical parameterization process within the PBL in
1167 the model, has been well proposed and developed by previous generations, but the development has
1168 been slower in recent years, few new theories have been proposed and almost no new schemes have
1169 been put into the model or the existing schemes have rarely been improved. Most of the previous
1170 studies have evaluated the PBL parameterization scheme, but many of them focus on a particular
1171 case in a certain region and lack of universality. This study makes up for this deficiency and provides
1172 a comprehensive discussion on the evaluation and uncertainty analysis of the PBL parameterization

scheme, hoping to give some reference to the model users. The future development of the PBL parameterization scheme needs to start from the theoretical mechanism, go deeper into the PBL parameterization scheme, and have a deeper understanding of the PBL parameterization, even if it is only for one scheme, or the improvement of one parameter. And for China's self-developed GRAPES model, the introduction and improvement of PBL parameterization schemes need to be selected, rather than a brain to write all the schemes, in fact, many schemes are almost not measured and used.

Code and data availability

The source code of WRF version 3.9.1 can be found on the following website: https://www2.mmm.ucar.edu/wrf/users/download/, and the model settings file is named "3.9.1_namelist.input", which can be found in the Supplement. In addition, the hourly meteorological observation data and L-band radiosonde observation data provided by the Chinese Academy of Meteorological Sciences, are available at https://doi.org/10.5281/zenodo.7792241 (Jia et al., 2023).

Author contributions

Development of the ideas and concepts behind this work was performed by all the authors. Model execution, data analysis and paper preparation were performed by WJ. XZ and HW provide computing resources, and offer advice and feedback. YW, DW, and JZ support the data. WZ, LZ, LG, YL, JW, YY, and YL provides suggestions. All authors contributed to the manuscript.

Competing interests

The authors declare that they have no conflict of interest.

Acknowledgements.

The work was carried out at the National Supercomputer Center in Tianjin, and the calculations were performed on TianHe-1 (A).

Financial support

This research is supported by NSFC Major Project (42090031), NSFC Project (U19A2044), Basic Research Fund of CAMS (2023Y003).

1202   Reference

1203   Acevedo, O. C., Mahrt, L., Puhales, F. S., Costa, F. D., Medeiros, L. E., andDegrazia, G. A.
1204   Contrasting structures between the decoupled and coupled states of the stable boundary
1205   layer. *Quarterly Journal of the Royal Meteorological Society, 142*(695), 693-702.
1206   doi:10.1002/qj.2693. 2015
1207   Atkinson, B. W., andZhang, W. J. Mesoscale shallow convection in the atmosphere. *Reviews of
1208   Geophysics, 34*(4), 403-431. doi:10.1029/96rg02623. 1996
1209   Avolio, E., Federico, S., Miglietta, M. M., Lo Feudo, T., Calidonna, C. R., andSempreviva, A. M.
1210   Sensitivity analysis of WRF model PBL schemes in simulating boundary-layer variables
1211   in southern Italy: An experimental campaign. *Atmospheric Research, 192*, 58-71.
1212   doi:10.1016/j.atmosres.2017.04.003. 2017
1213   Bauer, P., Thorpe, A., andBrunet, G. The quiet revolution of numerical weather prediction. *Nature,*
1214   *525*(7567), 47-55. doi:10.1038/nature14956. 2015
1215   Blackadar, A. K. The vertical distribution of wind and turbulent exchange in a neutral atmosphere.
1216   *Journal   of   Geophysical   Research   (1896-1977),   67*(8),   3095-3102.
1217   doi:10.1029/JZ067i008p03095. 1962
1218   Bougeault, P., andLacarrere, P. Parameterization of Orography-Induced Turbulence in a
1219   Mesobeta--Scale Model. *Monthly Weather Review, 117*(8), 1872-1890. doi:10.1175/1520-
1220   0493(1989)117<1872:Pooiti>2.0.Co;2. 1989
1221   Broxton, P. D., Zeng, X., Sulla-Menashe, D., andTroch, P. A. A Global Land Cover Climatology
1222   Using MODIS Data. *Journal of Applied Meteorology and Climatology, 53*(6), 1593-1605.
1223   doi:10.1175/jamc-d-13-0270.1. 2014
1224   Chen, F., andDudhia, J. Coupling an Advanced Land Surface–Hydrology Model with the Penn
1225   State–NCAR MM5 Modeling System. Part I: Model Implementation and Sensitivity.
1226   *Monthly   Weather   Review,   129*(4),   569-585.   doi:10.1175/1520-
1227   0493(2001)129<0569:Caalsh>2.0.Co;2. 2001
1228   Cohen, A. E., Cavallo, S. M., Coniglio, M. C., andBrooks, H. E. A Review of Planetary Boundary
1229   Layer Parameterization Schemes and Their Sensitivity in Simulating Southeastern U.S.
1230   Cold Season Severe Weather Environments. *Weather and Forecasting, 30*(3), 591-612.
1231   doi:10.1175/waf-d-14-00105.1. 2015
1232   Deardorff, J. W. Stratocumulus-capped mixed layers derived from a three-dimensional model.
1233   *Boundary-Layer Meteorology, 18*(4), 495-527. doi:10.1007/BF00119502. 1980
1234   Diaz, L. R., Santos, D. C., Käfer, P. S., Iglesias, M. L., da Rocha, N. S., da Costa, S. T. L., et al.
1235   Reanalysis profile downscaling with WRF model and sensitivity to PBL parameterization
1236   schemes over a subtropical station. *Journal of Atmospheric and Solar-Terrestrial Physics,*
1237   *222*, 105724. doi:10.1016/j.jastp.2021.105724. 2021

1238 Ding, H., Cao, L., Jiang, H., Jia, W., Chen, Y., andAn, J. Influence on the temperature estimation
1239   of the planetary boundary layer scheme with different minimum eddy diffusivity in WRF
1240   v3.9.1.1. *Geoscientific Model Development, 14*(10), 6135-6153. doi:10.5194/gmd-14-6135-
1241   2021. 2021

1242 Emery, C., Liu, Z., Russell, A. G., Odman, M. T., Yarwood, G., andKumar, N. Recommendations
1243   on statistics and benchmarks to assess photochemical model performance. *J Air Waste*
1244   *Manag Assoc, 67*(5), 582-598. doi:10.1080/10962247.2016.1265027. 2017

1245 Falasca, S., Gandolfi, I., Argentini, S., Barnaba, F., Casasanta, G., Di Liberto, L., et al. Sensitivity
1246   of near-surface meteorology to PBL schemes in WRF simulations in a port-industrial area
1247   with   complex   terrain.   *Atmospheric   Research,   264*,   105824.
1248   doi:10.1016/j.atmosres.2021.105824. 2021

1249 Ferrero, E., Alessandrini, S., andVandenberghe, F. Assessment of Planetary-Boundary-Layer
1250   Schemes in the Weather Research and Forecasting Model Within and Above an Urban
1251   Canopy Layer. *Boundary-Layer Meteorology, 168*(2), 289-319. doi:10.1007/s10546-018-
1252   0349-3. 2018

1253 Grell, G. A., andDévényi, D. A generalized approach to parameterizing convection combining
1254   ensemble and data assimilation techniques. *Geophysical Research Letters, 29*(14), 38-31-
1255   38-34. doi:https://doi.org/10.1029/2002GL015311. 2002

1256 Gu, H., Jin, J., Wu, Y., Ek, M. B., andSubin, Z. M. Calibration and validation of lake surface
1257   temperature simulations with the coupled WRF-lake model. *Climatic Change, 129*(3), 471-
1258   483. doi:10.1007/s10584-013-0978-y. 2015

1259 He, J., Chen, D., Gu, Y., Jia, H., Zhong, K., andKang, Y. Evaluation of planetary boundary layer
1260   schemes in WRF model for simulating sea-land breeze in Shanghai, China. *Atmospheric*
1261   *Research, 278*, 106337. doi:10.1016/j.atmosres.2022.106337. 2022

1262 Hong, S.-Y., Noh, Y., andDudhia, J. A New Vertical Diffusion Package with an Explicit Treatment
1263   of   Entrainment   Processes.   *Monthly   Weather   Review,   134*(9),   2318-2341.
1264   doi:10.1175/mwr3199.1. 2006

1265 Hong, S.-Y., andPan, H.-L. Nonlocal Boundary Layer Vertical Diffusion in a Medium-Range
1266   Forecast   Model.   *Monthly   Weather   Review,   124*(10),   2322-2339.   doi:10.1175/1520-
1267   0493(1996)124<2322:Nblvdi>2.0.Co;2. 1996

1268 Hong, S.-Y., andShin, H. H. Analysis of Resolved and Parameterized Vertical Transports in
1269   Convective Boundary Layers at Gray-Zone Resolutions. *Journal of the Atmospheric*
1270   *Sciences, 70*(10), 3248-3261. doi:10.1175/jas-d-12-0290.1. 2013

1271 Hu, X.-M., Nielsen-Gammon, J. W., andZhang, F. Evaluation of Three Planetary Boundary Layer
1272   Schemes in the WRF Model. *Journal of Applied Meteorology and Climatology, 49*(9), 1831-
1273   1844. doi:10.1175/2010jamc2432.1. 2010

1274   Iacono, M. J., Delamere, J. S., Mlawer, E. J., Shephard, M. W., Clough, S. A., andCollins, W. D.
1275   Radiative forcing by long-lived greenhouse gases: Calculations with the AER radiative
1276   transfer models. *Journal of Geophysical Research: Atmospheres, 113*(D13).
1277   doi:https://doi.org/10.1029/2008JD009944. 2008

1278   Janjić, Z. I. The Step-Mountain Coordinate: Physical Package. *Monthly Weather Review, 118*(7),
1279   1429-1443. doi:10.1175/1520-0493(1990)118<1429:Tsmcpp>2.0.Co;2. 1990

1280   Janjić, Z. I. The Step-Mountain Eta Coordinate Model: Further Developments of the Convection,
1281   Viscous Sublayer, and Turbulence Closure Schemes. *Monthly Weather Review, 122*(5), 927-
1282   945. doi:10.1175/1520-0493(1994)122<0927:Tsmecm>2.0.Co;2. 1994

1283   Jia, W., andZhang, X. The role of the planetary boundary layer parameterization schemes on the
1284   meteorological and aerosol pollution simulations: A review. *Atmospheric Research, 239*.
1285   doi:10.1016/j.atmosres.2020.104890. 2020

1286   Jia, W., andZhang, X. Impact of modified turbulent diffusion of PM2.5 aerosol in WRF-Chem
1287   simulations in eastern China. *Atmos. Chem. Phys., 21*(22), 16827-16841. doi:10.5194/acp-
1288   21-16827-2021. 2021

1289   Jiménez, P. A., andDudhia, J. Improving the Representation of Resolved and Unresolved
1290   Topographic Effects on Surface Wind in the WRF Model. *Journal of Applied Meteorology
1291   and Climatology, 51*(2), 300-316. doi:10.1175/jamc-d-11-084.1. 2012

1292   Kusaka, H., Kondo, H., Kikegawa, Y., andKimura, F. A Simple Single-Layer Urban Canopy Model
1293   For Atmospheric Models: Comparison With Multi-Layer And Slab Models. *Boundary-
1294   Layer Meteorology, 101*(3), 329-358. doi:10.1023/A:1019207923078. 2001

1295   Ma, Z., Zhao, C., Gong, J., Zhang, J., Li, Z., Sun, J., et al. Spin-up characteristics with three types
1296   of initial fields and the restart effects on forecast accuracy in the GRAPES global forecast
1297   system. *Geoscientific Model Development, 14*(1), 205-221. doi:10.5194/gmd-14-205-2021.
1298   2021

1299   Mass, C. F., Ovens, D., Westrick, K., andColle, B. A. DOES INCREASING HORIZONTAL
1300   RESOLUTION PRODUCE MORE SKILLFUL FORECASTS?: The Results of Two
1301   Years of Real-Time Numerical Weather Prediction over the Pacific Northwest. *Bulletin of
1302   the American Meteorological Society, 83*(3), 407-430. doi:10.1175/1520-
1303   0477(2002)083<0407:Dihrpm>2.3.Co;2. 2002

1304   Mellor, G. L., andYamada, T. A Hierarchy of Turbulence Closure Models for Planetary Boundary
1305   Layers. *Journal of Atmospheric Sciences, 31*(7), 1791-1806. doi:10.1175/1520-
1306   0469(1974)031<1791:Ahotcm>2.0.Co;2. 1974

1307   Mellor, G. L., andYamada, T. Development of a turbulence closure model for geophysical fluid
1308   problems. *Reviews of Geophysics, 20*(4), 851-875. doi:10.1029/RG020i004p00851. 1982

1309   Meng Lu, Zhao Tianliang, Yang Xinghua, Liu Chong, He Qing, andJingxin, D. An assessment of

1310   atmospheric boundary layer schemes over the Taklimakan Desert hinterland. *Journal of*
1311   *the Meteorological Sciences, 38*(2), 157-166. 2018

1312 Miao, Y., Liu, S., Guo, J., Huang, S., Yan, Y., andLou, M. Unraveling the relationships between
1313   boundary layer height and PM(2.5) pollution in China based on four-year radiosonde
1314   measurements. *Environ Pollut, 243*(Pt B), 1186-1195. doi:10.1016/j.envpol.2018.09.070.
1315   2018

1316 Monahan, A. H., andAbraham, C. Climatological Features of the Weakly and Very Stably
1317   Stratified Nocturnal Boundary Layers. Part II: Regime Occupation and Transition
1318   Statistics and the Influence of External Drivers. *Journal of the Atmospheric Sciences,*
1319   *76*(11), 3485-3504. doi:10.1175/jas-d-19-0078.1. 2019

1320 Monin, A. S., andObukhov, A. M. Basic laws of turbulent mixing in the surface layer of the
1321   atmosphere. *Akad. Nauk SSSR Trud. Geofiz. Inst, 24*, 163-187. 1954

1322 Morrison, H., Thompson, G., andTatarskii, V. Impact of Cloud Microphysics on the Development
1323   of Trailing Stratiform Precipitation in a Simulated Squall Line: Comparison of One- and
1324   Two-Moment Schemes. *Monthly Weather Review, 137*(3), 991-1007.
1325   doi:10.1175/2008mwr2556.1. 2009

1326 Nakanishi, M., andNiino, H. An Improved Mellor–Yamada Level-3 Model with Condensation
1327   Physics: Its Design and Verification. *Boundary-Layer Meteorology, 112*(1), 1-31.
1328   doi:10.1023/B:BOUN.0000020164.04146.98. 2004

1329 Nielsen-Gammon, J. W., Hu, X.-M., Zhang, F., andPleim, J. E. Evaluation of Planetary Boundary
1330   Layer Scheme Sensitivities for the Purpose of Parameter Estimation. *Monthly Weather*
1331   *Review, 138*(9), 3400-3417. doi:10.1175/2010mwr3292.1. 2010

1332 Noh, Y., Cheon, W. G., Hong, S. Y., andRaasch, S. Improvement of the K-profile Model for the
1333   Planetary Boundary Layer based on Large Eddy Simulation Data. *Boundary-Layer*
1334   *Meteorology, 107*(2), 401-427. doi:10.1023/A:1022146015946. 2003

1335 Oke, T. R., Mills, G., Christen, A., andVoogt, J. A. (2017). *Urban Climates.* United States of America:
1336   Cambridge University

1337 Paulson, C. A. The Mathematical Representation of Wind Speed and Temperature Profiles in the
1338   Unstable Atmospheric Surface Layer. *Journal of Applied Meteorology and Climatology,*
1339   *9*(6), 857-861. doi:10.1175/1520-0450(1970)009<0857:Tmrows>2.0.Co;2. 1970

1340 Persson, P. O. G., Walter, B., Bao, J. W., andMichelson, S. A. (2001). *3 VALIDATION OF*
1341   *BOUNDARY-LAYER PARAMETERIZATIONS IN A MARITIME STORM USING*
1342   *AIRCRAFT DATA.*

1343 Pleim, J. E. A Combined Local and Nonlocal Closure Model for the Atmospheric Boundary Layer.
1344   Part I: Model Description and Testing. *Journal of Applied Meteorology and Climatology,*
1345   *46*(9), 1383-1395. doi:10.1175/jam2539.1. 2007

1346   Shen, W., Lu, Z., Ye, G., Zhang, Y., Chen, S., andXu, J. (2022). Exploring the Impact of Planetary
1347   Boundary Layer Schemes on Rainfall Forecasts for Typhoon Mujigae, 2015. *Atmosphere,*
1348   *13*(2). doi:10.3390/atmos13020220

1349   Stull, R. B. Transilient Turbulence Theory. Part I: The Concept of Eddy-Mixing across Finite
1350   Distances. *Journal of Atmospheric Sciences, 41*(23), 3351-3367. doi:10.1175/1520-
1351   0469(1984)041<3351:Tttpit>2.0.Co;2. 1984

1352   Stull, R. B. (1988). *Turbulence Closure Techniques. An introduction to boundary layer meteorology*
1353   (Vol. 6). London: Atmospheric Sciences Library.

1354   Sun, J., Mahrt, L., Banta, R. M., andPichugina, Y. L. Turbulence Regimes and Turbulence
1355   Intermittency in the Stable Boundary Layer during CASES-99. *Journal of the Atmospheric*
1356   *Sciences, 69*(1), 338-351. doi:10.1175/jas-d-11-082.1. 2012

1357   Troen, I. B., andMahrt, L. A simple model of the atmospheric boundary layer; sensitivity to surface
1358   evaporation. *Boundary-Layer Meteorology, 37*(1), 129-148. doi:10.1007/BF00122760. 1986

1359   Vignon, E., van de Wiel, B. J. H., van Hooijdonk, I. G. S., Genthon, C., van der Linden, S. J. A.,
1360   van Hooft, J. A., et al. Stable boundary-layer regimes at Dome C, Antarctica: observation
1361   and analysis. *Quarterly Journal of the Royal Meteorological Society, 143*(704), 1241-1253.
1362   doi:10.1002/qj.2998. 2017

1363   Wang, C., Shen, Y., Luo, F., Cao, L., Yan, J., andJiang, H. Comparison and analysis of several
1364   planetary boundary layer schemes in WRF model between clear and overcast days.
1365   *Chinese J. Geophys. (in Chinese), 60*(3), 924-934. 2017

1366   Williams, P. D. Modelling climate change: the role of unresolved processes. *Philos Trans A Math*
1367   *Phys Eng Sci, 363*(1837), 2931-2946. doi:10.1098/rsta.2005.1676. 2005

1368   Wyngaard, J. C., andBrost, R. A. Top-Down and Bottom-Up Diffusion of a Scalar in the Convective
1369   Boundary Layer. *Journal of Atmospheric Sciences, 41*(1), 102-112. doi:10.1175/1520-
1370   0469(1984)041<0102:Tdabud>2.0.Co;2. 1984

1371   Xie, B., Fung, J. C. H., Chan, A., andLau, A. Evaluation of nonlocal and local planetary boundary
1372   layer schemes in the WRF model. *Journal of Geophysical Research: Atmospheres, 117*(D12).
1373   doi:10.1029/2011JD017080. 2012

1374   Zhang, D., andAnthes, R. A. A High-Resolution Model of the Planetary Boundary Layer—
1375   Sensitivity Tests and Comparisons with SESAME-79 Data. *Journal of Applied Meteorology*
1376   *and Climatology, 21*(11), 1594-1609. doi:10.1175/1520-
1377   0450(1982)021<1594:Ahrmot>2.0.Co;2. 1982

1378   Zhou, B., Zhu, K., andXue, M. A Physically Based Horizontal Subgrid-Scale Turbulent Mixing
1379   Parameterization for the Convective Boundary Layer. *Journal of the Atmospheric Sciences,*
1380   *74*(8), 2657-2674. doi:10.1175/jas-d-16-0324.1. 2017

1381